# A methodology based on GEOBIA and WorldView-3 imagery to derive vegetation indices at tree crown detail in olive orchards

Francesco Solano , Salvatore Di Fazio, Giuseppe Modica

University of Reggio Calabria, Loc. Feo di Vito, 89129, Reggio Calabria, Italy

# A methodology based on GEOBIA and WorldView-3 imagery to derive Vegetation Indices at tree crown detail in olive orchards

**Abstract**

Precision agriculture (PA) is becoming an essential practice for the implementation of sustainable agriculture that encompasses the efficient use of resources and a systematic crops monitoring. The increasing temporal and spatial resolution of satellite imagery, coupled with their availability and decreasing costs, create new possibilities for generating accurate datasets on different crops variables, more frequently available as ready-to-use data. The availability of very high-resolution (VHR) satellite imagery, such as the WorldView-3 (WV-3), leads to the advanced potential of satellite Remote Sensing (RS), becoming in the last decade one of the main data source in precision agriculture (PA). In the broad overview of these procedures, geographic object-based image classification (GEOBIA) techniques, gained broad interest as methods to produce geographic information in GIS-ready format. In this paper, methodologies for a semiautomatic process workflow is presented, providing olive tree crown detection in two different olive orchards in Calabria (Italy), collected by means of GEOBIA procedures, in order to investigate olive tree spectral behavior and the reliability of WW-3 derived vegetation indices (VIs). The semi-automated classification method, accomplished by imagery pre-processing steps, may constitute an operational processing chain for mapping and monitoring olive orchards at tree scale detail. Five VIs were investigated: Normalized Difference Vegetation Index (NDVI), Modified Soil Adjusted Vegetation Index 2 (MSAVI 2), Normalized Difference Red Edge Vegetation Index (NDRE), Modified Chlorophyll Absorption Ratio Index Improved (MCARI2), and NDVI2. The obtained results were statistically tested and their accuracy assessed. Thematic accuracy ranges from 95.33% to 96% in both study areas with an overall tree detection rate of 96.8%. Statistical analysis showed that the major differences in spectral behavior, over different plots of the investigated olive orchards, are mainly due to the component of the red-infrared regions of the electromagnetic spectrum (EM), where the red-edge becomes important in assessing the state of general vigor. Moreover, the proposed methodology increases the possibility of detecting tree stress at earlier stages and the benefits of using satellite-based approaches in terms of: larger area coverage, less processing and operator interaction coupled with more spectral information, thus reducing the need to collect costly reference data sampling.

**Keywords:** Olive trees' crown extraction, Vegetation Indices (VIs); Worldview-3 (WV-3); geographic object-based image classification (GEOBIA); spectral behavior; Precision Agriculture (PA), Olive orchards; Satellite Remote Sensing

## 1. Introduction

Olive (*Olea europaea* L.) is one of most ancient plants cultivated by human communities. Its domestication dates back prior 6000 BC (in the areas of present Syria and Turkey) while the earliest archaeological testimonies related to olive-oil production (presses and mortars found in Israel) date to around 4500 BC. In the Mediterranean area, the cultivation of olive acquired great importance when it reached the mainland and the islands of Greece, particularly Crete. Here, it soon became an important driver of development for the Minoan civilization that dominated the Mediterranean basin from around 2700 to 1500 BC. When the Greek civilization expanded throughout the Mediterranean basin, the cultivation of olive and the production of olive oil became an important economic activity also in the new colonies of Magna Graecia, established in southern Italy from the VIII century BC, and in the following Roman civilization. Olive oil, extracted in an ever more efficient way thanks to innovation in dedicated technology, had many and varied uses: culinary, as fuel for lamps, for lubrication, food preservation, cosmetics, ritual anointing. Olive-oil this way became, and still is, a recurring element in all the cultural expressions of the Mediterranean peoples (Foxhall, 2007; Tardi, 2014), as well as one of the main sources of income and employment (de Graaff and Eppink, 1999). Currently, olive groves are widespread in the Mediterranean Basin (Loumou and Giourga, 2003) and represent a recognized sign of several Mediterranean historical rural landscapes, also marking significantly their character (Di Fazio and Modica, 2018). Moreover, in the Mediterranean basin, falls the great majority of 9.4 million ha of olive groves cultivated globally (Vossen, 2007).

Presently, the Mediterranean area is the most important olive and olive oil world-producing region. With reference to average values of the last five years, world olive oil yearly production is about 3 million tons, 93% of which comes from the Mediterranean area (International Olive Council, 2018). An important role is played by four European Mediterranean countries, Spain, Italy, Greece and Portugal. Spain progressively increased its production since the late 1980s (Buckland and Gonzales, 2010), thanks to innovation, modernization and intensification of oliviculture, now being the world leader with 1.3 million tons olive oil produced, equal to 43% of world production, followed by Italy

84    (0.35 million tons, ~12% world production). Most of Italian production comes from Apulia and

85    Calabria, 48% and 17% respectively (ISMEA, 2018).

86    With reference to the period 2013-18, while the average yearly production of Spain largely exceeds

87    the national consumption, the quantity of olive oil produced in Italy is about 60% the oil consumed,

88    that is not enough to reach self-sufficiency. In Italy, therefore it is apparent the need to increase the

89    national olive oil production as well as to improve its quality; this, to fully match internal consumer's

90    demand, and better compete with other Mediterranean countries in export towards countries such as

91    USA and Japan where the Mediterranean diet and high quality extra-virgin olive oil are having a

92    growing popularity. In the framework of a continuously evolving global market, olive and olive oil

93    industries should introduce new and innovative technologies in order to enhance their productivity and

94    improve their competitiveness (Benalia et al., 2017). Precision agriculture (PA) methodologies and

95    technologies can be currently considered as the most reliable and cost effective approach for achieving

96    both sustainable environmental management and efficient crop production, thus revealing themselves

97    as an important tool to support decision-making and improve the competitiveness of agriculture. The

98    recent and fast development in sensory technologies and the parallel progressive reduction of their

99    costs, have allowed ever more users to benefit from applications of PA. Agriculture represents an

100   important economic sector for the application of geographic information systems (GIS) and remote

101   sensing (RS) data and methods. Providing spatial segmentation and within-field variability

102   information, RS is one of the most powerful tool to monitor and manage field crops in the framework

103   of PA techniques (Sepulcre-Cantò et al., 2005). PA also benefits from RS derived information on plant

104   photosynthetic processes at various spatial and temporal scales (Kumar and Monteith, 1981; Prince,

105   1990; Veroustraeate et al., 2002). Plants' biophysical characteristics can be spectrally characterized by

106   vegetation indices (VIs) which can be defined as radiometric measurements without unit. They are

107   calculated as ratios or differences of two or more bands in the visible (VIS), near infra-red (NIR) and

108   short wave IR (SWIR) portion of the EM spectrum remotely detected by satellite, aerial and terrestrial

109   platforms. VIs are primarily intended for use in PA (Roberts et al., 2011) and most of them measure

110   the reflectance of red, NIR and the red-edge (RE) portion of the EM spectrum in the reflectance curve

111   that describes the transition from absorption by chlorophyll to dispersion. The use of NIR

measurements, characterized by a greater penetration through the canopy cover, allows for estimating the total amount of green material (Modica et al., 2019). Measurement in the RE region allow these indices to be more sensitive to minor changes in vegetation health, particularly in dense vegetation conditions (Pauly, 2014).

The usefulness of a VI is determined by its high correlation with plants biophysical parameters and the low sensitivity to the factors that hinder the interpretation of RS data, such as soil background, terrain roughness, non-photosynthetic plant elements, atmosphere, viewing and illumination geometry (Wojtowicz et al., 2016). The increasing geometric and temporal resolution and the positional accuracy of satellite sensors in the last fifteen years, however, allow the assessment of problems such as vegetation health, drought stress, fruit yield assessment and flooding (Bausch and Khosla, 2010; Calderón et al., 2015, 2013; Calvão and Palmeirim, 2004; Hunt et al., 2013; Villalobos et al., 2006; Wallace et al., 2004). The primary platforms used to obtain RS imagery were satellites and piloted aircrafts, but they frequently did not deliver adequate spatial and temporal resolutions (Nebikera et al., 2008). The advent of very high-resolution (VHR) imagery such as those provided by WorldView-3 (WV-3) (DigitalGlobe Inc., www.digitalglobe.com), has led to the advanced potential of satellite RS, which in the near future will probably become the main methodology of data acquisition from agricultural field parcels. In addition to the development of vehicles and sensors for the acquisition of VHR imagery, even multispectral imaging technologies have been implemented to provide increasingly efficient and reliable information extraction methods. In the broad overview of these procedures, geographic object-based image classification (GEOBIA) techniques, gained broad interest as methods to produce geographic information in GIS-ready format (Blaschke et al., 2014). This approach considers not only the identification of the ground coverage at the pixel level, but also the organization of these pixels in groups (segments) that correspond to objects in the real world (Blaschke, 2010; Chepkochei, 2011). The analysis of scientific literature shows that several researches deal with the use of WV imagery coupled with GEOBIA techniques. Different research topics ranging from tree species classification to greenhouse detection were investigated (Aguilar et al., 2013; Alrassi et al., 2016; Chepkochei, 2011; Chuang and Shiu, 2016; Gaertner, 2017; Majid et al., 2016; Mutanga et al., 2015; Shahi et al., 2017; Shojanoori et al., 2016; Waser et al., 2014). On the other hand,

140     literature reports very few experiences dealing with the application of WV-3 in studying the

141     physiological status of individual tree (Anderson et al., 2018; Koenig and Gueguen, 2016;

142     Palchowdhuri et al., 2018; Rahman et al., 2018; Robson et al., 2017). This is mainly due to the very

143     recent availability of WV-3 imagery (August 2014) and to the high cost required to access these data

144     (Zartaloudis et al., 2015).

145     Taking into consideration the aforementioned research findings, the present paper has three main

146     research goals: a) to provide a semiautomatic workflow aimed at the olive tree crown detection and

147     extraction by means of GEOBIA techniques; b) to investigate the reliability of WW-3 derived VIs in

148     analyzing olive trees' vegetative vigor without ground radiometric measures; c) to provide a quick and

149     cost saving procedure not needing expensive ground truths collection in the framework of PA

150     techniques.

151     The structure of the present paper is as follows. In section 2, the study areas are presented and

152     described, while section 3 deals with materials and methods, providing details on data processing

153     workflow, pre-processing steps (subsections 3.1-3.2), the analyzed VIs, and GEOBIA procedures

154     aimed at the tree crown extraction (subsections 3.3.-3.6). Section 4 is devoted to show the obtained

155     results, discussed in section 5 and, and finally, section 6, deals with conclusions and final remarks.

156

## 157    2. Study areas

158     The study was carried out in Calabria, a region characterized by high hydrogeological risk (Petrucci et

159     al., 2009), and in which olive groves assume a significant role in reducing rainfall's losses. These

160     systems include agro-forestry stands, traditional groves and new intensive orchards, with a high yield

161     variability due to the co-existence of extensive orchards with few trees per hectare and intensive ones

162     having more than 600 trees ha$^{-1}$ (Bernardi et al., 2016). In the region, which is located in the very

163     South of the Italian peninsula, the province of Reggio Calabria is the most representative. There, two

164     specialized olive orchards identified as A and B and managed according to organic farming methods

165     were selected to develop and evaluate our proposed method (Fig. 1). Both study areas were chosen in

166  relation to their extension and cultivation characteristics, they do not differ in crop management

167  system, while differ in tree shapes and dimensions, as well as according to the plantation age.

168
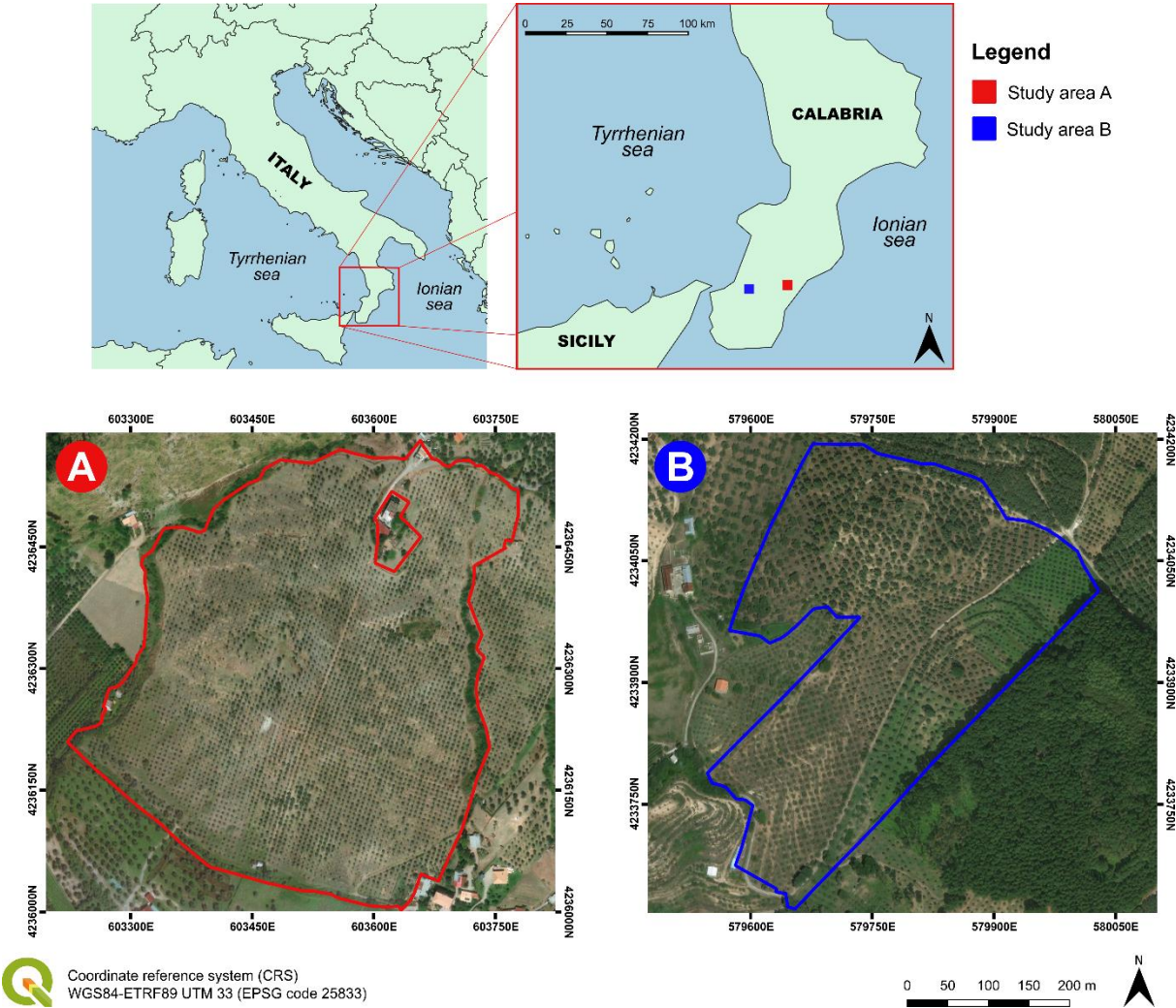


170  **Fig. 1.** Study areas localization based on high spatial resolution WorldView-3 satellite images presented in true color band
171  combination (RGB 5-3-2) (Acquisition date: A, 24 June 2016; B, 2 July 2016).
172

173  The orchards chosen are characterized as follows. Olive orchard A is located in in the municipality of

174  Gerace covering a surface of 21.42 ha. Cultivar is "Grossa di Gerace" and olive trees' age is about 20

175  years while a traditional single-tree 6m x 6m planting distance is adopted. Soil is mostly clay,

176  naturally grassy and periodically mowed in spring season, while irrigation is not adopted neither in

177  drought periods. The only treatments provided are based on copper during dormancy.

178  Olive orchard B is located in the municipality of Delianuova (Fig. 1) covering a surface of 14.28 ha.

179  Olive trees' age is about 15 years and mixed cultivars "Ottobratica" (80%) and "Leccino" (20%) are
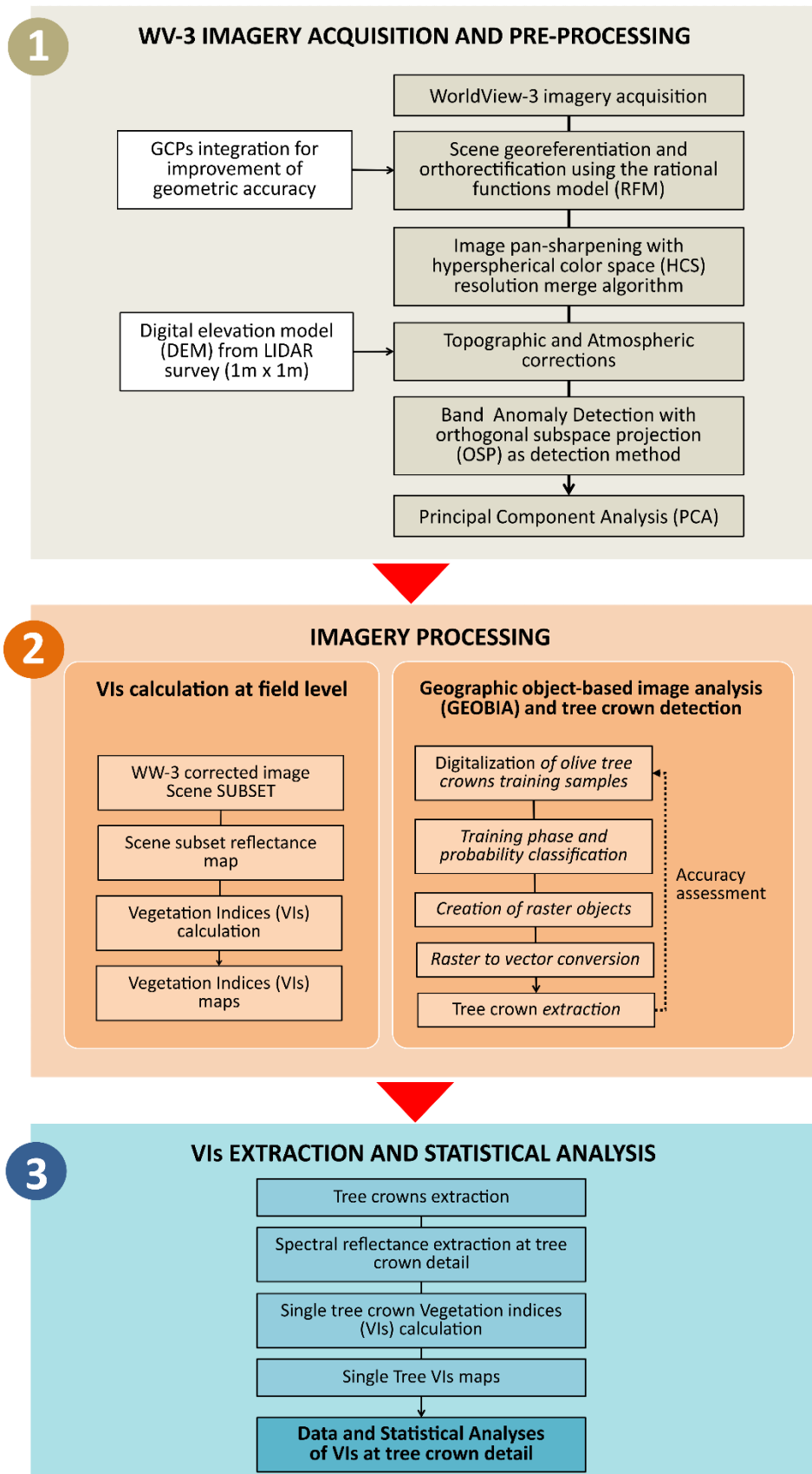
180 produced adopting a traditional single-tree 6m x 6m planting distance. Soil is mostly with medium

181 texture, naturally grassy and periodically mowed in spring, summer and autumn seasons, while

182 irrigation is not adopted even in drought periods. Also in this case, only copper treatments during

183 dormancy are provided.

184 Within each study area, 4 plots of 2150 m$^2$ (8 in total), respectively labelled as $A_1$, $A_2$, $A_3$, $A_4$ and $B_1$,

185 $B_2$, $B_3$, $B_4$, and with different potential productivity, were identified in order to deepen investigation

186 and compare spectral behavior at tree crown detail.

187

## 3.  Material and Methods

### 3.1   Data processing workflow

190 Having preliminarily defined a specific workflow in the spatial modeler environment in Erdas

191 Imagine® 2018 software (Fig. 2), we implemented a semi-automated geoprocessing operations based

192 on customized RS imagery processing procedures. The full procedure can be singled out in three main

193 phases: 1) WV-3 imagery acquisition and pre-processing analysis; 2) imagery processing trough

194 GEOBIA followed by tree crown detection and extraction, and generation of VIs maps; 3) VIs

195 extraction at tree crown detail and statistical analyses for the reliability assessment of the obtained

196 results.

**1 WV-3 IMAGERY ACQUISITION AND PRE-PROCESSING**

WorldView-3 imagery acquisition

GCPs integration for improvement of geometric accuracy

Scene georeferentiation and orthorectification using the rational functions model (RFM)

Image pan-sharpening with hyperspherical color space (HCS) resolution merge algorithm

Digital elevation model (DEM) from LIDAR survey (1m x 1m)

Topographic and Atmospheric corrections

Band Anomaly Detection with orthogonal subspace projection (OSP) as detection method

Principal Component Analysis (PCA)

**2 IMAGERY PROCESSING**

**VIs calculation at field level**

WW-3 corrected image Scene SUBSET

Scene subset reflectance map

Vegetation Indices (VIs) calculation

Vegetation Indices (VIs) maps

**Geographic object-based image analysis (GEOBIA) and tree crown detection**

Digitalization *of olive tree crowns training samples*

*Training phase and probability classification*

*Creation of raster objects*

*Raster to vector conversion*

Tree crown *extraction*

Accuracy assessment

**3 VIs EXTRACTION AND STATISTICAL ANALYSIS**

Tree crowns extraction

Spectral reflectance extraction at tree crown detail

Single tree crown Vegetation indices (VIs) calculation

Single Tree VIs maps

**Data and Statistical Analyses of VIs at tree crown detail**

197

198 **Fig. 2.** A synthetic flow-chart showing the implemented semi-automated processing workflow to derive vegetation indices
199 (VIs) at tree crown details from WordlView-3 (WW3) imagery.
200

## 3.2 Satellite Data Acquisition and pre-processing steps

A pair of WV-3 satellite images were acquired on 24 June 2016 for study area A and on 2 July 2016

for B and processed. WV-3 dataset consisted of eight multispectral bands and one panchromatic band

images at 16 bit of radiometric resolution (Table 1). Both images were first georeferenced according to

the coordinate reference system (CRS) WGS84-ETRF89 UTM 33 (EPSG code 25833) then

orthorectified using the rational function model (RFM). The model was refined by integrating ground

control points (GCPs) and consequent improvement of geometric accuracy for orthorectified data.

To increase the original geometrical resolution of MS bands (1.24 m), the hyperspherical color space

(HCS) resolution merge pan-sharpening algorithm (Padwick et al., 2010) was applied to merging them

with the pan band (0.31 m). HCS was used taking into consideration its capability in preserving the

original image spectral information (Dahiya et al., 2013; Padwick et al., 2010). Further, a 7×7

smoothing filter was applied, followed by the output resampling by means of the nearest neighbor

interpolation algorithm.

**Table 1 -** WorldView-3 sensor wavelength bands [nm] and relative ground sample distance [GSD] details (centered wavelength in brackets).

| Band | Wavelength [nm] | Ground sample distance (GSD) [m] |
|---|---|---|
| Panchromatic | 450-800 | 0.31 |
| Coastal blue | 400-450 (425) | 1.24 |
| Blue | 450-510 (480) | |
| Green | 510-580 (545) | |
| Yellow | 585-625 (605) | |
| Red | 630-690 (660) | |
| Red-edge | 705-745 (725) | |
| NIR-1 | 770-895 (835) | |
| NIR-2 | 860-1040 (950) | |

Classic corrections, i.e. topographic and atmospheric, were then performed using all WV-3 bands (1-

8), by means of the atmospheric correction module (ATCOR Workflow) of ERDAS Imagine® 2018.

Therefore, the original digital numbers (DNs) were converted into spectral radiance at sensor's

222  aperture ($L_A$) for correcting to surface reflectance. To calibrate the images, gain and offset calibration

223  values provided with imagery metadata were used (Balthazar et al., 2012; Vanonckelen et al., 2014).

224  ATCOR3 algorithm is based on MODTRAN atmospheric radiative transfer code and allows to set

225  different weather conditions, and solar zenith and azimuth angles. In our case, a rural aerosol model

226  for spring and summer seasons with a visibility distance of 10 km was the applied to four terrain files

227  (slope, aspect, sky view, and shadow cast) obtained from a digital elevation model (DEM) (Richter,

228  1998, 1997) by a modified Minnaert topographic correction that use a set of empirical rules (Richter et

229  al., 2009), considering rugged terrain effects in the correction process. As input, we used a 1 m × 1 m

230  DEM derived from an aerial LiDAR dataset surveyed in 2011. Finally, an anomaly detection (AD)

231  process was carried out to identify pixels that have a spectral signature markedly different from most

232  other pixel spectra in the image by mean of the orthogonal subspace projection (OSP) as detection

233  method.

234  In order to support the subsequent classification phases adding texture detail to the pixel classifier, a

235  principal component analysis (PCA) spectral transformation was then adopted. A PCA provides a

236  reduction of correlation among bands' reflectance values, by rotating the axes of the original feature

237  space coordinate system to new orthogonal axes (called principal component, PC) maximizing the data

238  variance, therefore making the data more interpretable (Jolliffe, 2002). In order to select the right

239  number of components that account for a high proportion of the data variance, we calculated PCs for

240  all eight WV-3 bands, also obtaining the covariance matrix and the eigenvalues for each of them.

241  Generally, most of the variance is collected in the first three PCs (Richards and Jia, 2006). In our case,

242  we selected the first two PCs considering that for both imagery their account for more than 97% of the

243  data variance (Table 3).

244

## 3.3   Geographic object-based image analysis (GEOBIA) and tree crown extraction

246  The GEOBIA approach was implemented in Erdas Imagine® Objective as semi-automatic process

247  with minimum user intervention, able to extract single olive tree crown and to eliminate the spectral

248  disturbances of background, independently of the plantation pattern. The tree crown model detection

249     was defined with a pixel cue classifier based on multi Bayesian network so that the different output

250     classes could directly interact with each other (Fig. 3). As input data, the atmospherically corrected

251     WV-3 imagery, and the PC1 and PC2 layers were used for both A and B study areas. Preliminarily, for

252     each study area, a set of 30 olive tree crowns representing our feature training reference samples, and a

253     set of background samples, were manually digitized as vector polygons. PC1 and PC2 data layer were

254     added as input to the Identity cue to use as a metric to the Pixel Classifier. Then, a single feature

255     probability (SFP) method was applied to the WV-3 imagery to calculate probability metrics (ranging

256     from 0 to 1) of the input multispectral image, comparing its pixel values with those of the digitized

257     polygons. Higher and lower probability values were assigned to pixels whose values were similar or

258     significantly different from the values of pixels in the non-background training samples, respectively.

259     In the training phase, pixels identified with training polygons belonging to single olive trees were used

260     to compute pixel cue metrics for training the pixel classifier for each study area. The selected pixel

261     were compared, during this process node, to the training pixels obtaining a pixel probability layer (Fig.

262     3) representing the probability in which each pixel's value is an object of interest (i.e. an olive tree

263     crown). Then, a threshold/clump function was applied on the pixel probability layer by keeping only

264     those pixels presenting a percentage probability greater than or equal to the threshold value of 0.95, in

265     our case. Each created raster object is a clump object (i.e., the belonging pixels share a common ID

266     class in the attribute table).

267     Based on a raster object pixel distribution, we set a 5 x 5 circular kernel size to expand the raster

268     object distribution with a minimum object size of 40 pixels, and then specify a minimum clump size of

269     40 pixels. Clumps smaller than the specified number were eliminated. Raster objects were

270     automatically vectorized based on the associated probability metrics and smoothed in shape, applying

271     a smoothing factor of 0.70 (Fig. 3).

272     For each "tree object polygon", size property and a measure of probability membership to the group of

273     tree vector objects was performed by means of an object classifier using training sample distribution

274     parameters such as mean, minimum, maximum and standard deviation values. The automated

275     extraction phase was then performed to measure how closely the selected polygons match the training

276  objects. Objects processed passed through the object cue metrics calculation such as shape (circularity)

277  and size (area) with a pixel probability weight set to 95%.

278
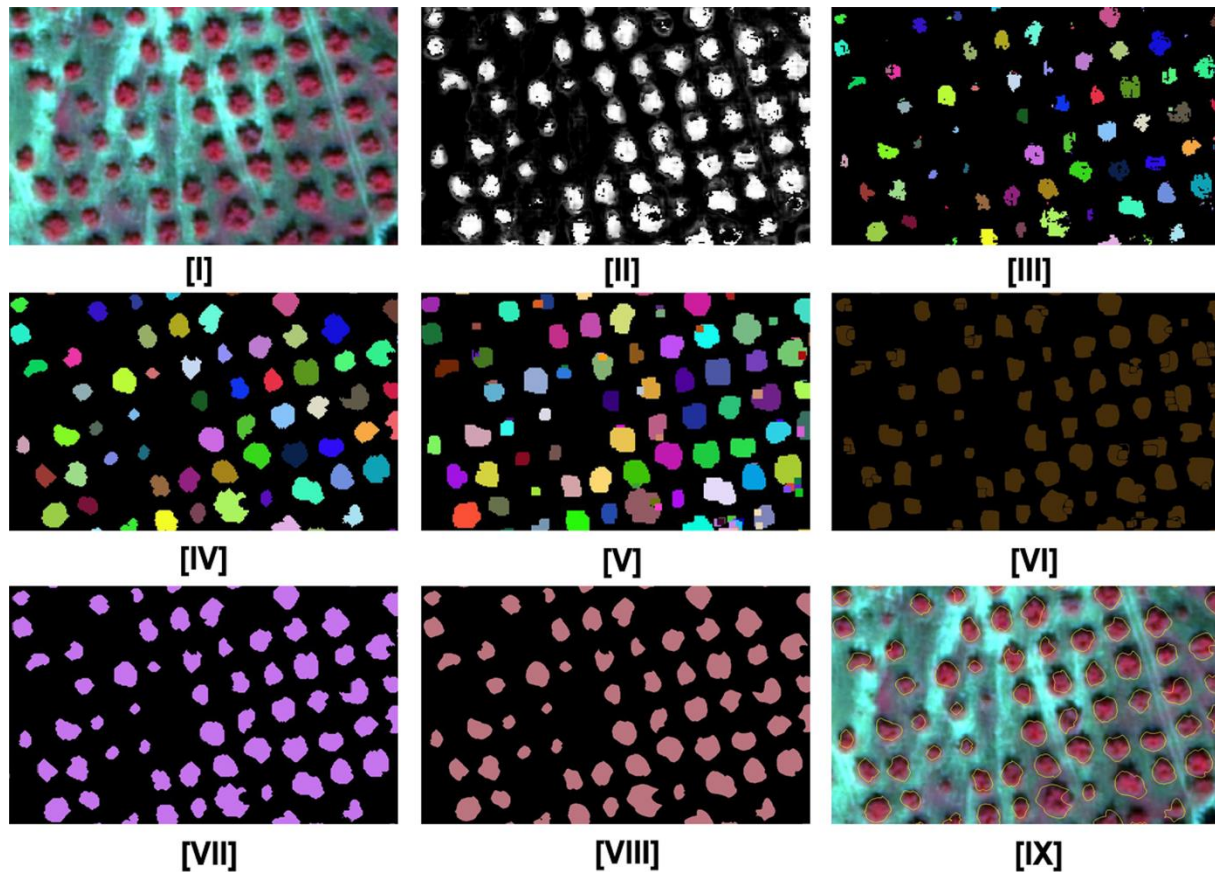


280  **Fig. 3.** Geographic object-based image analysis (GEOBIA) sequenced feature model process nodes for the extraction of olive
281  tree crowns. (I): a subset of the corrected WorldView-3 (WV-3) satellite imagery, presented in a false infrared color band
282  combination (RGB 7-5-3); (II): raster pixel processor; (III): raster object creator; (IV-V): raster object operators; (VI): rater to
283  vector conversion; (VII): vector object operator; (VIII): vector object processor; (IX): extracted olive tree crown boundaries
284  [yellow line] overlapped on the input image.
285

286  The process ended with a vector clean-up operation with a probability filter function that removed all

287  vector objects whose zonal probability mean was less than the specified minimum probability by

288  remodeling the existing vector objects (Fig. 3). This value was set to 95%. The resulting vector objects

289  represent the extracted olive tree crowns (Fig. 3).

290

### 3.4   GEOBIA and tree crown extraction accuracy

292  To assess the tree crown extraction accuracy, all olive trees' crowns falling in the 8 plots ($A_1$- $A_4$ and

293  $B_1$- $B_4$) were digitized by on-screen photointerpretation and used as reference data (Erikson, 2004;

294    Larsen et al., 2011; Wang et al., 2004). To ensure the correct geolocalization of each tree falling in the

295    eight plots, a set of ground control points (ground truths) was defined collecting the position of each of

296    them by means of a differential GNSS (planimetric accuracy = ±0.05 m). These points were then used

297    as reference data in the photointerpretation stages display their position on the pan-sharpened WV-3

298    imagery (Koc-San et al., 2018; Rahman et al., 2018; Robson et al., 2017; Srestasathiern and Rakwatin,

299    2014). The accuracy was assessed as object-based evaluation by comparing the total number of

300    correctly detected trees with these reference data. Evaluation was performed by simply counting trees

301    correctly detected or missing, basing on two independent samples: one for the recall (*r*) and another

302    for the precision (*p*). Recall indicates the omission error while precision indicates the commission

303    error (Li et al., 2012). The overall accuracy was obtained by the F-score (Eq. 1):

304    $$F\text{-}score = 2 \times \frac{(r \times p)}{(r+p)} \qquad (1)$$

305    Where:

306    $$r = \frac{TP}{TP + FN}$$

307    $$p = \frac{TP}{TP + FP}$$

308    F-score represents the harmonic mean of recall and precision and it's a measure of the overall

309    accuracy (Goutte and Gaussier, 2005; Lu et al., 2014; Sokolova et al., 2006). These performance

310    indicators were evaluated considering: true positives (TP), i.e. correctly detected trees; false positives

311    (FP), i.e. erroneously detected trees; and false negatives (FN), i.e. trees not detected.

312    Following the work of Ok et al. (2013), an overlapping threshold of 60% was then defined to assess

313    the obtained accuracies between the reference and the detected object.

314    To determine the relationship between correctly detected trees and reference data, a regression

315    analysis was implemented with R statistical software (R Core Team, 2017). The quality of fitted linear

316    regression model was evaluated based on the coefficient of determination ($R^2$) and the root mean

317    square error (RMSE) according to equation 2:

318    $$\text{RMSE} = \sqrt{\frac{1}{n}\sum_{i=1}^{n}(x_i - y_i)^2} \qquad (2)$$

319    where, $x_i$ represents reference tree data and $y_i$ the detected tree crown. The significance was also

320    computed.

321    Furthermore, a confusion matrix was used to evaluate the overall 8 plots classification accuracy

322    (Congalton, 1991; Congalton and Green, 2008) obtaining an overall accuracy and the Kappa

323    coefficient (K) as expression of the accuracy in terms of omission/commission errors. To that purpose,

324    in each plot of the two study areas, a set of 10 randomly distributed sample points was defined.

325

326    **3.5    Investigated Vegetation Indices (VIs)**

327    In order to investigate the biophysical characteristics of olive trees, a set of five VIs was defined by

328    selecting those ones (Table 2) based on reflectance bands sensitive to the combined effects of

329    chlorophyll concentration, surface and vegetation canopy architecture. These VIs provide a reliable

330    measure of the photosynthetic material, crucial in understanding the vegetation vigor (Vincini et al.,

331    2008). NDVI, with the normalized combination of its formulation is the most popular VI (Pettorelli,

332    2013), capable to measure healthy vegetation using the highest chlorophyll absorption and reflectance

333    regions and whose values range from -1 to 1. However, NDVI can saturate in multi-layered dense

334    vegetation, when the leaf area index (LAI) reaches higher values (Haboudane et al., 2004; Maselli et

335    al., 2012; Ortega-Farías et al., 2016; Rouse et al., 1974; Tucker, 1979; Zheng and Moskal, 2009).

336    The modified soil adjusted vegetation index 2 (MSAVI2) is similar to the NDVI, but mitigate the soil

337    background effects. In its first formulation, this was obtained by using an adjustment factor (*L*), which

338    is a function of the vegetation density and often requires prior knowledge. In the second formulation

339    of the index, instead, the *L* factor was replaced by a self-regulating factor (Qi et al., 1994). MSAVI2

340    offers good performances with sparse vegetation, where the ground remains particularly visible

341    through the foliage (Eitel et al., 2007; Haboudane et al., 2004; Hunt et al., 2012).

342    NDRE index is a modification of NDVI and its applications include PA, forest monitoring, and

343    identification of vegetation stress (Cammarano et al., 2014; Fitzgerald, 2010; Hunt et al., 2012;

344    Siegmann et al., 2012).

345 NDRE has values ranging from -1 to 1 and differs from NDVI as it uses wavelengths along the Red-

346 Edge (RE) region. It exploits the vegetation sensitivity to RE to small variations in the canopy foliage

347 content, the canopy cover degree and senescence.

348

349 **Table 2 -** Formulation of the five vegetation indices (VIs) used in the present research.

| Index denomination | Index formula* | References |
|---|---|---|
| Normalized Difference Vegetation Index (**NDVI**) | $\dfrac{(\rho NIR1 - \rho RED)}{(\rho NIR1 + \rho RED)}$ | (Rouse et al., 1974) |
| Modified Soil Adjusted Vegetation Index 2 (**MSAVI 2**) | $\dfrac{2\rho NIR1 + 1 - \sqrt{(2\rho NIR1 + 1)^2 - 8(\rho NIR1 - \rho RED)}}{2}$ | (Broge and Leblanc, 2001; Qi et al., 1994) |
| Normalized Difference Red Edge Vegetation Index (**NDRE**) | $\dfrac{(\rho NIR1 - \rho RedEdge)}{(\rho NIR1 + \rho RedEdge)}$ | (Barnes et al., 2000) |
| Modified Chlorophyll Absorption Ratio Index Improved (**MCARI2**) | $\dfrac{1.5[2.5(\rho NIR1 - \rho RED) - 1.3(\rho NIR1 - \rho GREEN)]}{\sqrt{(2 \times \rho NIR1 + 1)^2 - (6 \times \rho NIR1 - 5 \times \sqrt{\rho RED}) - 0.5}}$ | (Haboudane et al., 2004) |
| Normalized Difference Vegetation Index 2 (NDVI2) | $\dfrac{(\rho NIR2 - \rho RED)}{(\rho NIR2 + \rho RED)}$ | (Eckert,2012; Pu et al., 2012; Wolf, 2012) |

350 *in all formulas, $\rho$ is the reflectance at the given wavelength.

351

352 The modified chlorophyll absorption ratio index improved (MCARI2) is one of several CARI indices

353 identifying the relative abundance of chlorophyll; like MCARI (Daughtry, 2000), it is considered a

354 good indicator of LAI. It incorporates an adjustment factor for the soil background, while preserving

355 sensitivity to LAI and resistance to the influence of chlorophyll (Eitel et al., 2007; Haboudane et al.,

356 2004; Hunt et al., 2012; Main et al., 2011). Thanks to the availability of a NIR2 band, the NDVI2

357 index (Eckert, 2012; Wolf, 2012) was used as a specific band ratio suitable for WV-3 imagery, which

358 values range from -1 to 1. Given any other multispectral indices system, a red band and a NIR band

359 shows the low and high level of vegetation reflectance values, respectively. In the NDVI2, band ratio

360 between the red coupled with the NIR2 band, which has a higher value than traditional broad NIR

361 bands, should produce higher NDVI values (Ng et al., 2017; Wolf, 2012).

As described, VIs maps for the two study-areas were obtained in the spatial modeler environment in

Erdas Imagine® 2018 suite, applying the standard formulations (Table 2) and masking them to the

geographical extent of each study area (Fig. 2). Final maps were built in QGIS 3.4 Madeira (Fig. 5-6).

## 3.6 Statistical Analysis of olive tree spectral signature and derived VIs

To corroborate research findings and further considerations, a statistical analysis was applied to all

calculated VIs. To this end, analyses were performed on all extracted VIs within the defined 8 plots

($A_1$- $A_4$ and $B_1$- $B_4$) using the extracted  tree crown vector derived from GEOBIA, in order to separate

the real cultivated areas from other parts (Fig. 3). For each plot, all trees falling inside were chosen as

statistic samples and, for each crown, basic statistics of VIs values (i.e., mean and standard deviation)

were calculated. The mean spectral signature of each plot was also computed and correlation among

bands was estimated by a correlation matrix. Single band reflectance values were evaluated using box

and whisker plots. Significance was computed using a two-tailed t test with n-2 degrees of freedom.

Aiming to assess how suitable VIs are to describe crops condition, we were interested in identifying

the regions of the EM spectrum in where olive trees most differ from each other, so that the index can

be representative of a real growth condition. For this purpose, one-way analysis of variance (ANOVA)

test was used to verify the statistical difference between trees in mean reflectance value in each

waveband and in each plot. The ANOVA tested the following hypothesis:

$$H_0 = \rho_1 = \rho_2 = \cdots \rho_n$$

$$H_1 = Not\ all\ \rho_n(i)\ are\ equal$$

where $\rho_n$ represents the mean reflectance of the n-th tree (n = 1, 2, 3, …13) and $i$ denotes the

waveband. Rejection of the null hypothesis ($H_0$) indicates the wavebands, at a 95% (p-value <0.05)

confidence level, in which the spectral signature differs statistically. $H_0$ rejection was followed by

pairwise multiple comparisons with the post-hoc Tukey HSD test. By counting the number of pairs

whose differences are statistically significant on each waveband, it is possible to identify the spectral

regions where the olive trees most differ, evidencing the wavebands that may have high discriminative

effects on VI's value. First, normality and homoscedasticity (i.e., homogeneity of variances) of the

reflectance values across each waveband were verified with Levene's test and Shapiro-Wilk test.

389     Where Levene's test was significant (i.e., it showed unequal variances), then the unequal-variance

390     (Welch F test) version of ANOVA (Moder, 2010) and the non-parametric Kruskal Wallis test for

391     taking control of values with non-normal distribution, were used. In these last cases, a Mann-Whitney

392     *U* test (Zar, 1996) was used as post-hoc pairwise comparison. Statistical analyses were performed with

393     R statistical software (R Core Team, 2017).

394

## 4. Results

396     **4.1 GEOBIA classification accuracy**

397     As described in paragraph 3.4, all olive trees' crowns falling in the 8 plots ($A_1$- $A_4$ and $B_1$- $B_4$) were

398     digitized by on-screen photointerpretation, thus representing our reference data, and compared to those

399     extracted by means of GEOBIA classification. To digitize these reference data, the image band

400     composition which proved to be as the most effective in revealing contrast and properties that were not

401     visually evident from the other false colors image was the RGB 7-6-5 (NIR1, Re, R) (Fig. 4).

402     The PCA analysis showed that the PCs axis derived from all for all the WV-3 bands, which explain

403     >95% of the variance (cumulative proportion of all components) were represented by PC1 and PC2 for

404     a total variance percentage of 97.4 in A and 98.5 in B (Table 3), such that only these two components

405     were used in GEOBIA tree crown classification process.

406

407 **Table 3 -** Results of principal component analysis (PCA) of WV-3 imagery of study areas A and B, showing the Eigenvalues
408 obtained from the covariance matrix and the percentage variance contribution of each principal component (PC).

| PC | A | | | B | | |
|---|---|---|---|---|---|---|
| | Eigenvalue | %Variance | Cumulative Variance | Eigenvalue | %Variance | Cumulative Variance |
| 1 | 25455.122 | 61.22 | 61.22 | 60209.084 | 80.56 | 80.56 |
| 2 | 15025.964 | 36.14 | 97.36 | 13390.535 | 17.92 | 98.48 |
| 3 | 469.852 | 1.13 | 98.49 | 541.596 | 0.72 | 99.20 |
| 4 | 256.930 | 0.62 | 99.18 | 361.990 | 0.48 | 99.68 |
| 5 | 200.421 | 0.48 | 99.66 | 151.383 | 0.20 | 99.88 |
| 6 | 123.278 | 0.30 | 99.96 | 49.487 | 0.07 | 99.95 |
| 7 | 41.494 | 0.03 | 99.99 | 29.601 | 0.04 | 99.99 |
| 8 | 8.666 | 0.01 | 100 | 7.745 | 0.01 | 100 |

409

410
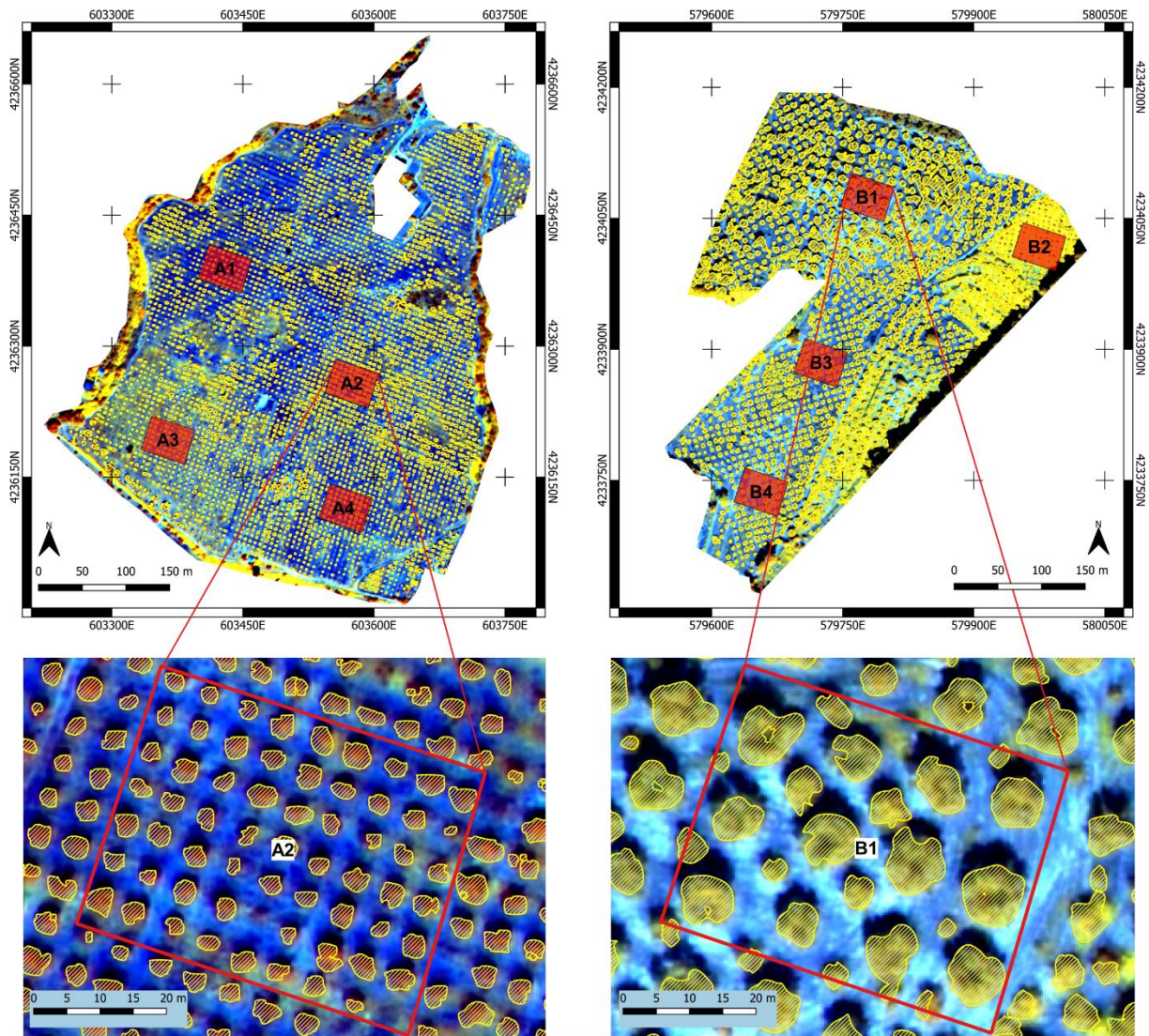
**Legend**

■ Plots for accuracy assessment

□ Detail of plots A2 and B1

▨ Olive tree crowns

**Fig. 4.** WV-3 scene subset of the two olive orchards (acquisition date: [A] 24 June 2016; [B] 2 July 2016) showed with vegetation enhancement color band combination (RGB 7-6-5). In each study area, in red, are highlighted the four plots defined for accuracy assessment of geographic object-based image classification (GEOBIA) and for statistical analyses of spectral behavior of olive trees [Top left, study area A. Top right, study area B. Down left and down right, image detail of plot $A_2$ and $B_1$, respectively, with superimposed (in yellow) the polygonal boundaries of tree crowns obtained through GEOBIA classification and extraction].

Results showed that most of the trees were correctly classified and extracted in all plots of both study areas. The accuracy assessment showed an overall accuracy of 95% in study area A and 98% in study area B (Table 4). The final object probability layer, in which each pixel's value represents the probability that it is the feature of interest, reached the probability value of 82% in study area A and

423    78% in study area B. Crown dimensional analysis confirmed a marked difference on tree structure

424    between study areas, with a more vigorous structure in olive orchard B.

425

426    **Table 4 -** Accuracy assessment of classified study area images derived from GEOBIA and olive sample trees cue metrics [(±
427    n): ± st.dev].

| Sample plot | Pixel probability | Area [m$^2$] | Circularity | Probability |
|---|---|---|---|---|
| A$_1$ | 0.70 (±0.07) | 2.50 (±1.27) | 0.81 (±0.07) | 0.76 (±0.11) |
| A$_2$ | 0.78 (±0.06) | 6.51 (±1.58) | 0.79 (±0.07) | 0.82 (±0.11) |
| A$_3$ | 0.78 (±0.09) | 4.54 (±2.40) | 0.84 (±0.08) | 0.89 (±0.12) |
| A$_4$ | 0.80 (±0.06) | 5.27 (±1.37) | 0.80 (±0.07) | 0.83 (±0.11) |
| *Overall plot accuracy (%)* | 95.33 | | | |
| *Overall plot K coefficient* | 0.9513 | | | |
| B$_1$ | 0.73 (±0.09) | 31.10 (±19.08) | 0.80 (±0.08) | 0.83 (±0.15) |
| B$_2$ | 0.54 (±0.08) | 11.20 (±6.16) | 0.75 (±0.08) | 0.73 (±0.12) |
| B$_3$ | 0.75 (±0.08) | 16.48 (±7.05) | 0.76 (±0.08) | 0.78 (±0.12) |
| B$_4$ | 0.74 (±0.08) | 14.55 (±7.35) | 0.87 (±0.07) | 0.79 (±0.13) |
| *Overall plot accuracy (%)* | 98.67 | | | |
| *Overall plot K coefficient* | 0.9724 | | | |

428

429    The total number of olive trees in the 8 plots were 359, 347 of which were correctly extracted, missing

430    11 trees and falsely detecting 1 tree (Table 5). In study area A, characterized by smaller olive trees,

431    values of r (omission error) varies from 0.91 to 0.98 (overall value 0.95) while p value (commission

432    error) is 1. The F-score, which considers both r and p, varies from 0.95 to 0.99 (overall value of 0.97).

433    Whereas in study area B, with larger olive trees, value of r ranges from 0.95 to 1 (overall value of

434    0.97). The value of p is 1 in every plot except B2 (overall value of 0.97). The F-score ranges from 0.96

435    to 1 (overall value of 0.98). According to the obtained results, in plots B3 and B4 the best detection

436    rate at 100% was obtained, whilst plot A1 showed the worst detection rate (91.2%).

437    Very small trees (i.e., crown diameter <2 m) often tend to show a higher number of FN pixels because

438    part of their surrounding background is not included in the tree crown. This explains the decrease in

439    the accuracy obtained in plot A1 (F-score = 0.95), despite the promising success level for r (≈0.9). As

440    expected, large tree crowns tend to be more precisely detected. In some cases however, although very

441    small trees with a tree crown area (TCA) of 0.096 m$^2$ (9 pixels) were also correctly extracted, this

442    procedure tends to loose portions of them or, depending on their shape, divides them into two or more

443    objects (Fig. 3). The relationship between the number of reference trees and the number of extracted

444    trees for each plot are shown in Fig. 4. The relationship between the number of reference trees and the

445    number of extracted trees for each plot are shown in Fig. 5. The correlation result is relatively strong

446    with R2 = 0.986 and RMSE = 1.36, (p-value <0.001).

447

448    **Table 5 -** Results and accuracy indicators of the olive tree crown extraction (TP, true positive; FP, false positive; FN, false
449    negative; *r*, recall; *p*: precision).

| Plot ID | Number of trees | Number of detected trees | TP | FP | FN | r | p | F-score | Rates (TP/n° trees) [%] |
|---|---|---|---|---|---|---|---|---|---|
| *A₁* | 57 | 52 | 52 | 0 | 5 | 0.91 | 1.00 | 0.95 | 91.2 |
| *A₂* | 62 | 61 | 61 | 0 | 1 | 0.96 | 1.00 | 0.98 | 98.4 |
| *A₃* | 52 | 51 | 51 | 0 | 1 | 0.98 | 1.00 | 0.99 | 98.1 |
| *A₄* | 54 | 53 | 53 | 0 | 1 | 0.98 | 1.00 | 0.99 | 98.1 |
| *Overall A* | *225* | *217* | *217* | *0* | *8* | *0.95* | *1.00* | *0.97* | *96.4* |
| *B₁* | 23 | 22 | 22 | 0 | 1 | 0.95 | 1.00 | 0.97 | 95.6 |
| *B₂* | 47 | 44 | 44 | 1 | 2 | 0.95 | 0.97 | 0.96 | 93.6 |
| *B₃* | 33 | 33 | 33 | 0 | 0 | 1.00 | 1.00 | 1.00 | 100 |
| *B₄* | 31 | 31 | 31 | 0 | 0 | 1.00 | 1.00 | 1.00 | 100 |
| *Overall B* | *134* | *130* | *130* | *1* | *3* | *0.97* | *0.99* | *0.98* | *97.3* |
| *Overall* | *359* | *347* | *347* | *1* | *11* | *0.96* | *0.99* | *0.97* | *96.8* |

450

451



452
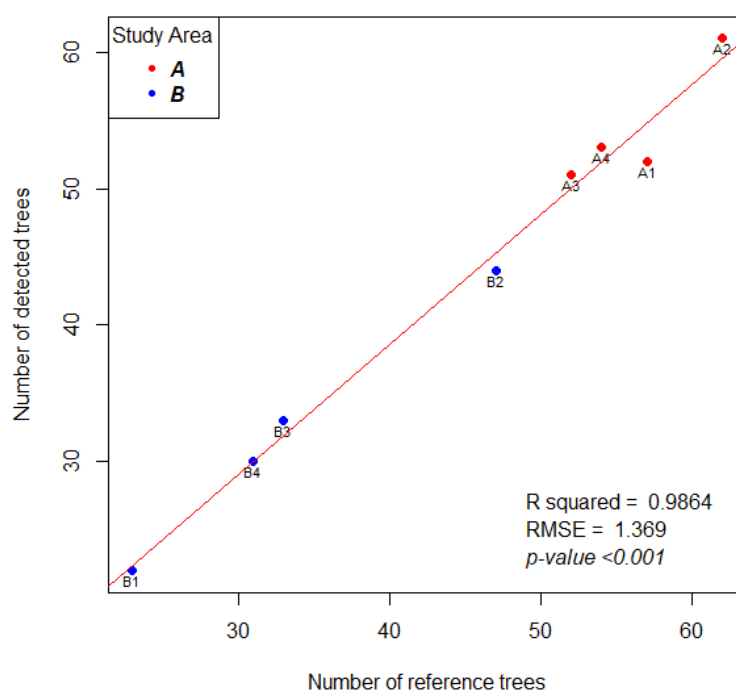
453    **Fig. 5.** Relationship between number of reference trees and number of correctly detected trees in the eight investigation plots.
454

## 4.2 Vegetation indices (VIs) maps

For both study areas, the spatial distribution of NDVI, MSAVI2, NDRE, MCARI2, and NDVI2

already showed significant pattern, i.e. zones with negative behavior are well recognizable (Figg. 6

and 7). However, all VIs maps were clearly affected by crown shadows of olive trees, and even small

changes in elevation of the terrain and herbaceous/shrub vegetation. At border zones of A olive

orchard, some continuous green pixels often appear, representing positive values of the indices, due to

the different oaks vegetation surrounding the olive orchard with continuous canopy cover. In B, some

areas where vegetation shows good values for all VIs are also discriminable in the field. These

features were well differentiated in the VIs color images.
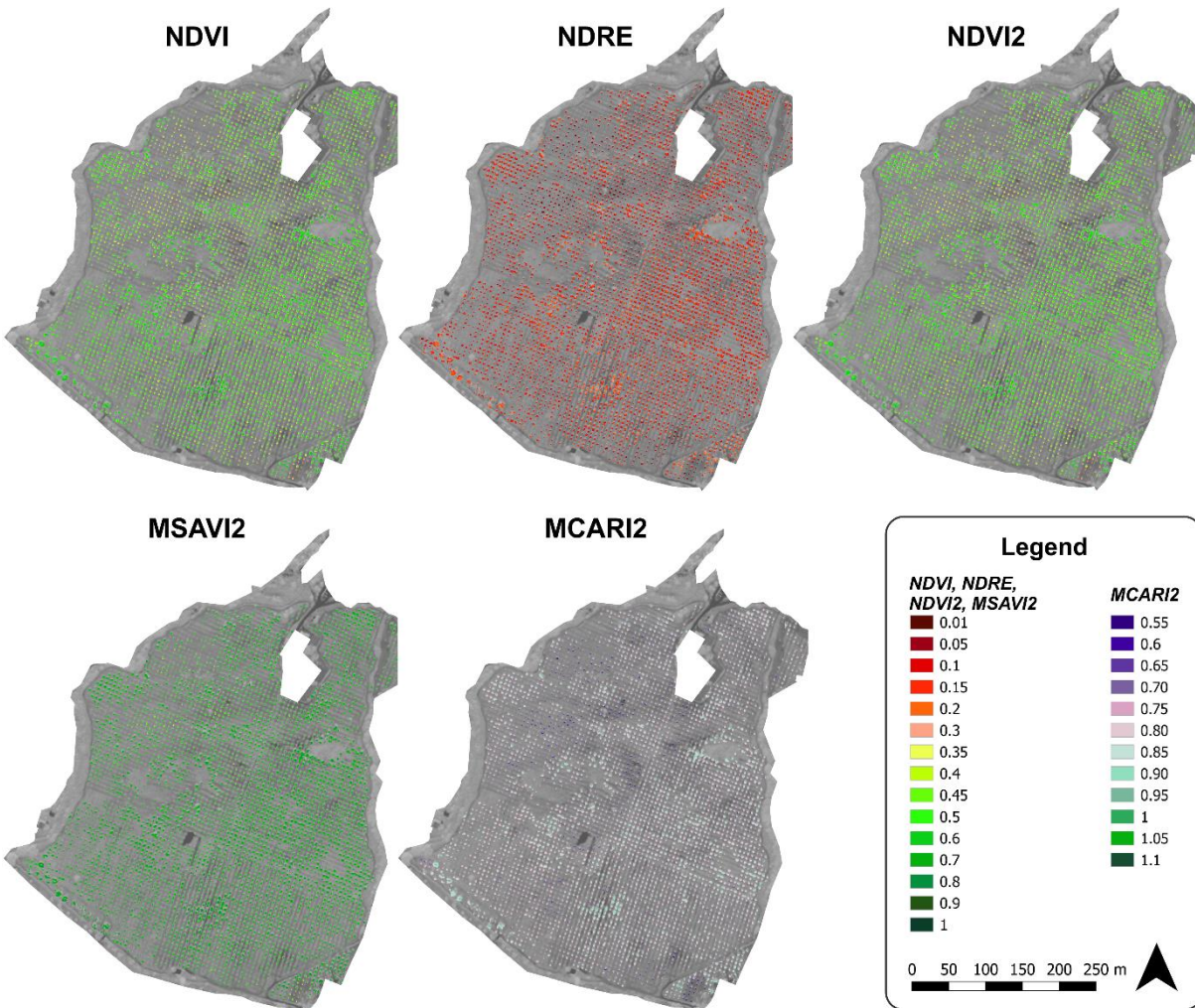


**Fig. 6.** Vegetation indices (VIs) maps of study area A

468  To confirm these qualitative considerations and to mitigate the effect of soil and herbaceous layer

469  background, statistical analyses were performed in the eight plots at tree crown detail, using the

470  derived GEOBIA tree crowns polygons as statistical unit (Table 5). For each plot, basic statistics of

471  indices values showed a different behavior of vegetation. In particular, the mean index value reflects a

472  mean productivity and biomass, whereas the standard deviation represents a measure of the spatial

473  variability in productivity (Rouse et al., 1974).

474  The mean value for all indices in study area A suggested that health condition of plot $A_2$, $A_3$ and $A_4$ is

475  better than $A_1$, as well as in study area B health condition of plot $B_3$, $B_4$ and $B_2$ is better than in plot $B_1$,

476  respectively. Concerning the NDVI, mean value ranges between 0.45 and 0.54 in A and between 0.62

477  and 0.77 in B showing higher level of biomass in the latter case.

478



479
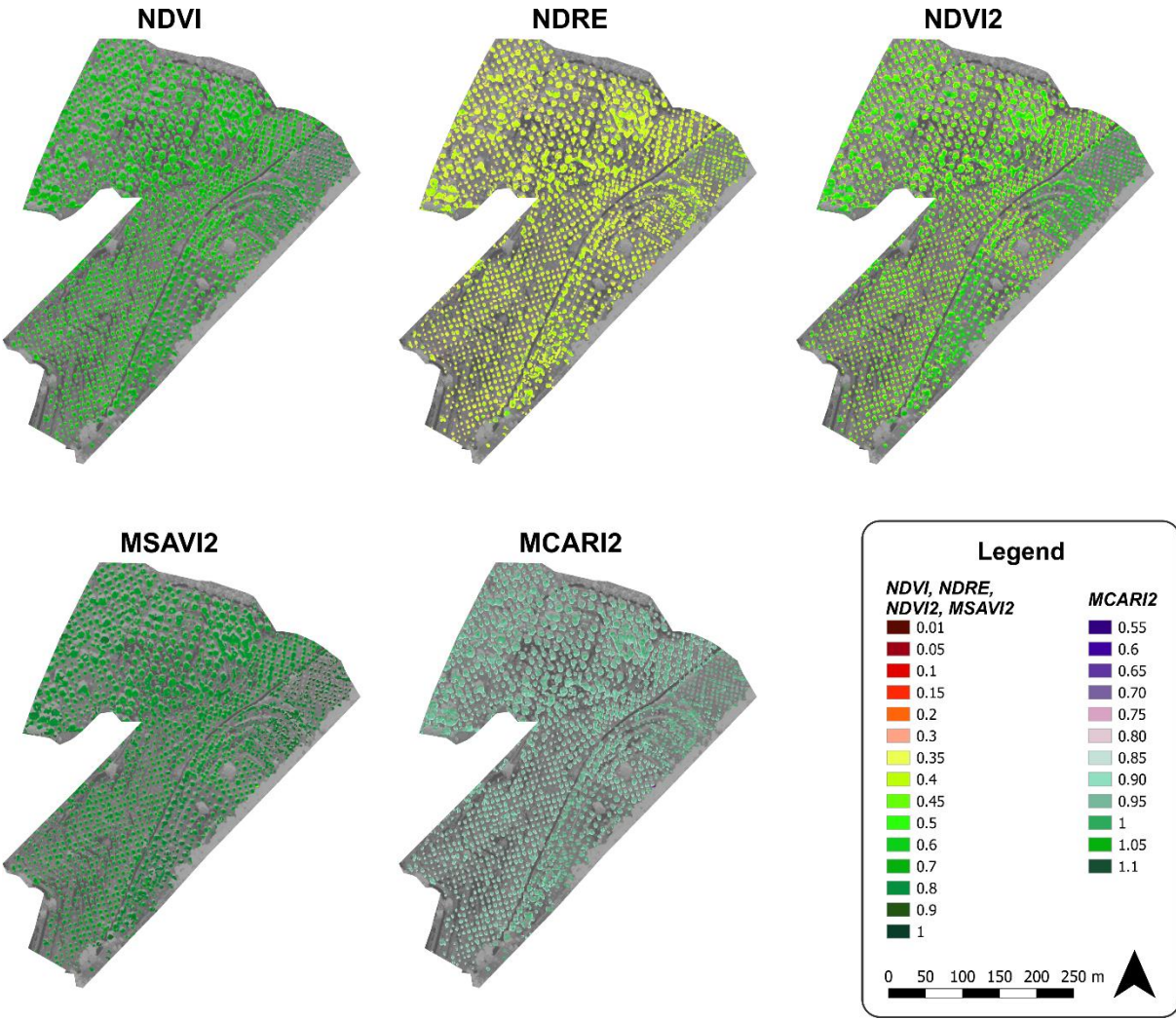
480  **Fig. 7.** Vegetation indices (VIs) maps of study area B

481 The increase in the mean value of MSAVI2, able to suppress the effects of soil background, is

482 approximately 25% in each plot, with the minimum increase of 19% in plot A2 and A4 and the

483 maximum of 27% in plot A1.

484 In B, the increase of MSAVI2 mean value is approximately of 17%, with the minimum increase of

485 12% in plot B2 and the maximum of 19% in plots B1 and B4. Given that the reflectance in RE band is

486 higher than in the red one, NDRE shows different value ranges compared to those of NDVI. The

487 NDRE reaches the maximum value in plots A2 and B2, whereas the minimum in plots A1 and B1

488 (Table 6), depending also on different foliage cellular structure.

489 The same behavior was found finally for MCARI2 and NDVI2 that prove again a situation similar to

490 the previous findings regarding the consistence of chlorophyll concentration.

491

492 **Table 6 -** Univariate statistics of Vegetation indices (VIs) map values, for each plot, inside A and B study areas

| Study area | Plot | NDVI | | MSAVI2 | | NDRE | | MCARI2 | | NDVI2 | |
|---|---|---|---|---|---|---|---|---|---|---|---|
| | | Mean | ± st.dev | Mean | ± st.dev | Mean | ± st.dev | Mean | ± st.dev | Mean | ± st.dev |
| A | $A_1$ | 0.45 | 0.03 | 0.62 | 0.03 | 0.12 | 0.02 | 0.77 | 0.03 | 0.49 | 0.03 |
| | $A_2$ | 0.55 | 0.03 | 0.68 | 0.03 | 0.15 | 0.02 | 0.82 | 0.02 | 0.54 | 0.03 |
| | $A_3$ | 0.54 | 0.02 | 0.68 | 0.01 | 0.14 | 0.02 | 0.80 | 0.02 | 0.53 | 0.02 |
| | $A_4$ | 0.54 | 0.03 | 0.67 | 0.02 | 0.13 | 0.02 | 0.81 | 0.02 | 0.53 | 0.02 |
| B | $B_1$ | 0.62 | 0.02 | 0.77 | 0.01 | 0.38 | 0.02 | 0.93 | 0.02 | 0.48 | 0.02 |
| | $B_2$ | 0.77 | 0.02 | 0.88 | 0.02 | 0.43 | 0.02 | 0.97 | 0.01 | 0.68 | 0.03 |
| | $B_3$ | 0.63 | 0.02 | 0.77 | 0.01 | 0.39 | 0.02 | 0.92 | 0.01 | 0.49 | 0.03 |
| | $B_4$ | 0.63 | 0.02 | 0.78 | 0.01 | 0.39 | 0.02 | 0.92 | 0.01 | 0.49 | 0.03 |

493

494 However, considering that previous statistic parameters are not able to fully describe data

495 distributions, the relative frequency distribution of VIs values was calculated for each plot at tree

496 crown detail (Figg. 8-9). To show an example of how structural vigor and chlorophyll concentration

497 vary among different plots, we compared NDRE and MCARI2 values' distribution of single tree

498 crown of the two study areas. Single tree crown VI of the plots confirmed that the trees of study area

499 A have a worse vegetative state than those in study area B. For all the VI maps, the graphics show that

500 the pixels belonging to area A are distributed over VI values lower than in area B, confirming again

501 the previous findings.
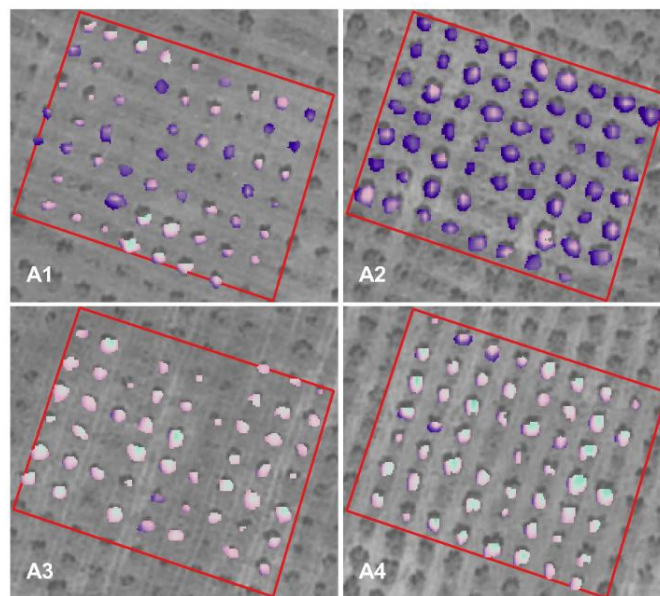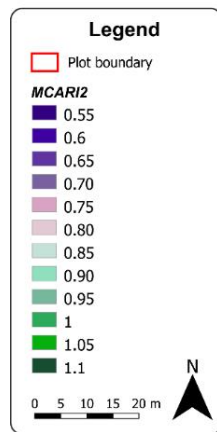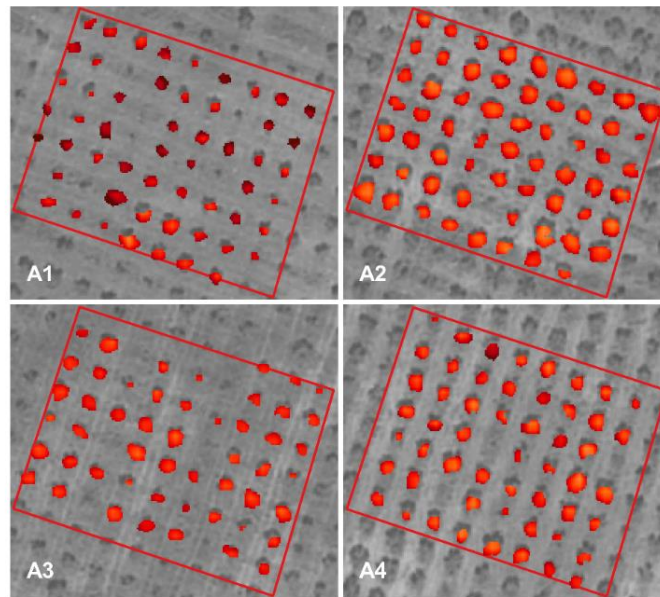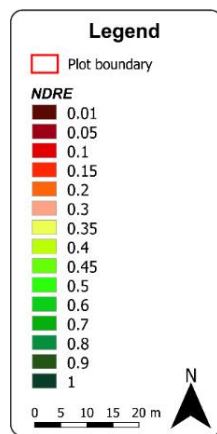
**Fig. 8.** Maps of Normalized Difference Red Edge (NDRE) and Modified Chlorophyll Absorption Ratio Index Improved (MCARI2) Vegetation indices (VIs) at tree crown detail of study area A.

Considering only NDRE, all the plots in the study area B reach the highest values, denoting a major structural vigor than those in study area A, trees differing mostly in crown dimension between the two study areas. Likewise, in B the MCARI2 values appear as higher than in A. The decrease of the values of MCARI2 in A may not be directly related to the state of health only but to the whole trees structures in the relative plots. This consideration is supported by the assessment made in the previous analysis, referring it to the only NDRE pixels value.

512
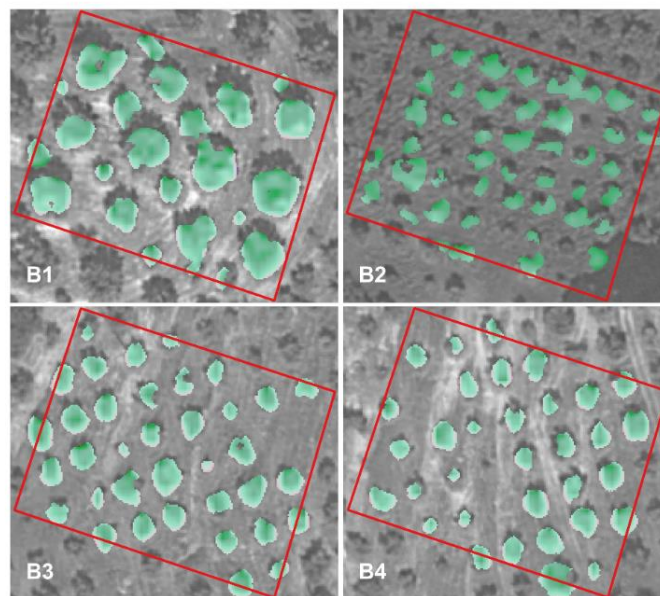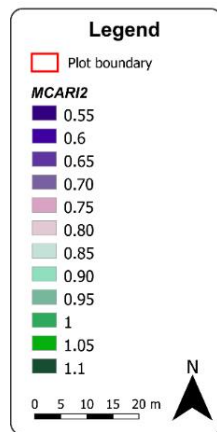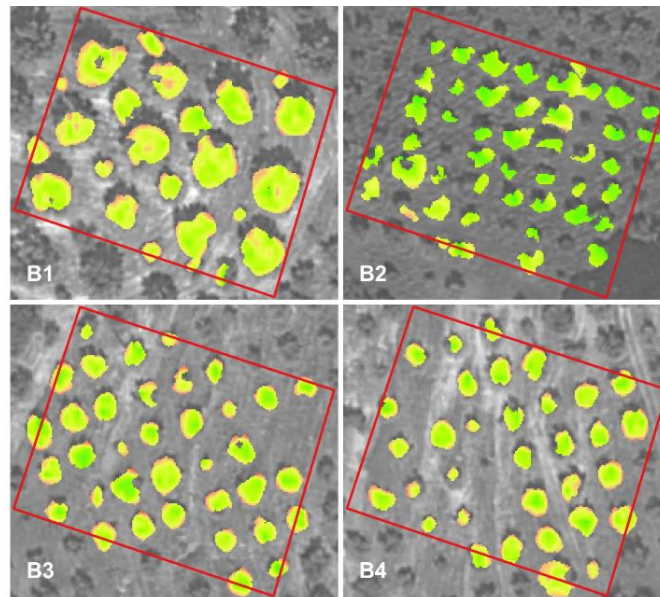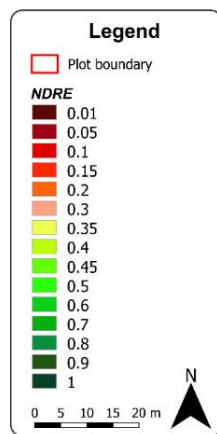
**Fig. 9.** Maps of Normalized Difference Red Edge (NDRE) and Modified Chlorophyll Absorption Ratio Index Improved
(MCARI2) Vegetation indices (VIs) at tree crown detail of study area B

515

## 4.3   Tree crown extraction and spectral behavior

A comparative analysis of the spectral properties revealed that most of the olive trees had similar

spectral intra-plot patterns. Most of the spectral variability is visible from the RE to NIR2 band while

the peak of reflectance was reached at RE band (Fig. 10). On the other hand, NIR values showed a

different range of reflectance spectra. The maximum reflectance was obtained in the NIR1 and NIR2

bands in B (Fig. 10). Analyzing these differences, and representing them according to the mean single

522    band reflectance values using box and whisker plots (Fig. 10), it was possible to better understand how

523    spectral signature changes between the eight plots.

524
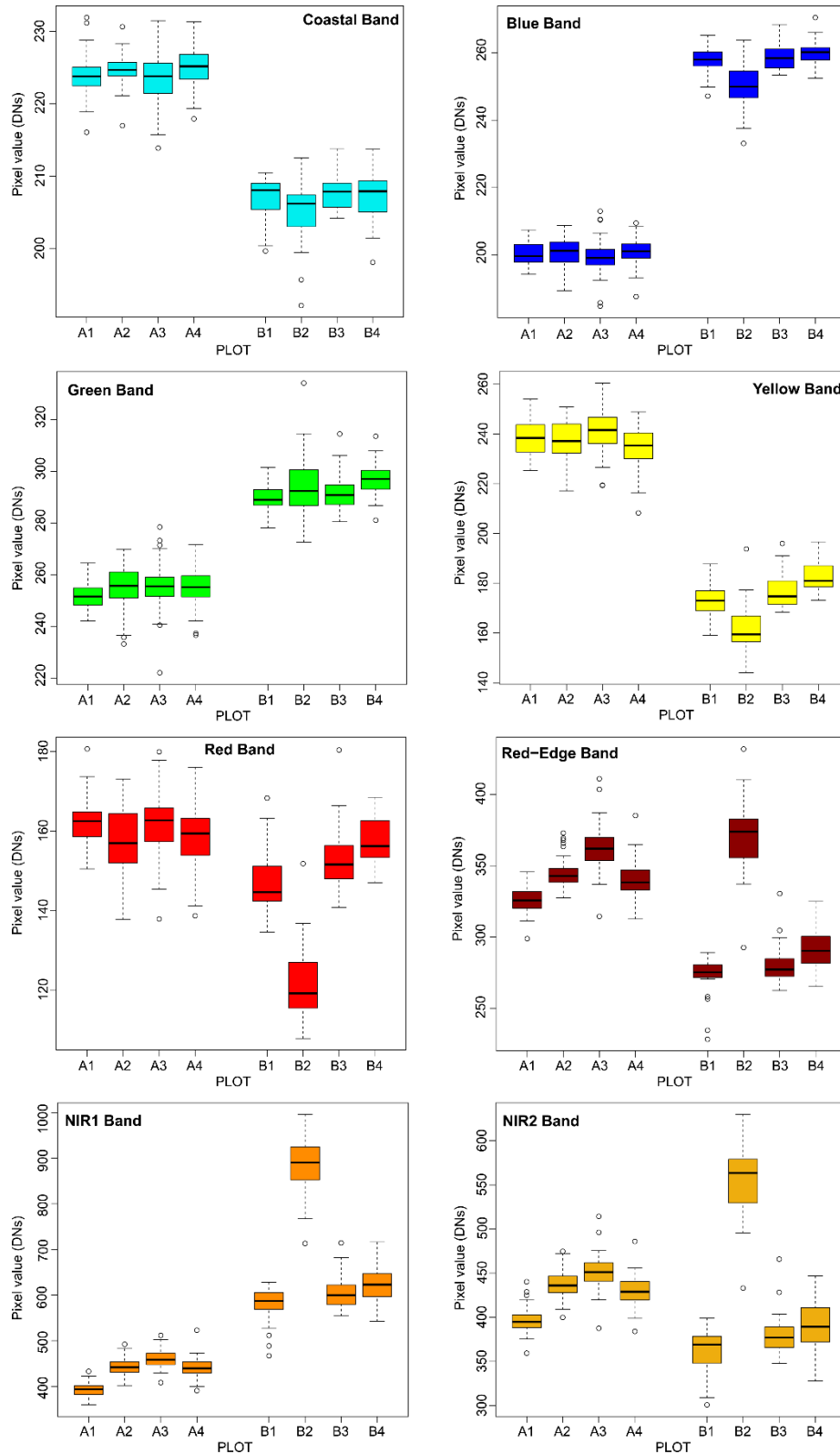


525    **Fig. 10.** Box-and-whisker plots of single WV-3 bands reflectance values variability in each study area plot (A1-A4 and B1-
526    B4).

527

528      About coastal and blue band in A, an overall low variability was found whilst highest values in the

529      green band confirmed major reflection in this region of the EM spectrum. In the Yellow band, the

530      highest pixel value was reached in plot $A_3$ that had the highest value in the RE, NIR1 and NIR2 band

531      too. RE, NIR1 and NIR2 reflectance peaks were reached in plot $A_3$ and $A_2$, confirming the best

532      vegetative state of olive trees that fall in to these plots, with the lowest reflectance in $A_1$ and $A_4$ in each

533      of these bands.

534      In general, the shape and distribution toward the spectral value is flat for all plots, with a minimal

535      green and yellow peak and different distribution patterns across 705-1040 nm wavelength. Differently,

536      in B coastal and yellow bands showed lower pixel value in these EM regions compared to A plots,

537      with highest values in the green and blue band. A similar distribution pattern is visible in the red band

538      with the lowest peak in plot $B_2$. The RE, NIR1 and NIR2 peak reflectance was reached in plot $B_2$

539      almost confirming a marked best vegetative state of the olive trees, with the lowest reflectance in $B_1$

540      in each of these bands. In principle, each B plot seems to display leaves with high photosynthetic

541      capacity to maximize direct beam radiation, resulting in higher NIR values.

542      Based on the correlation matrix, computed from the reference sample trees (Tables 7 and 8), it is

543      possible to identify some correlations between bands. For both study areas, the correlation among RE,

544      NIR1 and NIR2 bands was highly significant. In B it was found significant correlations also between

545      Yellow, Blue, Red and Coastal blue band. Within each group, correlations among bands are quite high

546      with an overall low *p*-value. Thus, these bands could provide redundant information.

547

548 **Table 7** - Pairwise correlations among the eight bands of WorldView-3 (WV-3) imagery, computed from the reference
549 sample trees of study area A. Correlation values are given in the lower triangle of the matrix, and the two-tailed probabilities
550 are given in the upper (Correlations >0.75 in bold letters, ns: no significance; *p<0.01, **p<0.05).

| A /<br>Band | Coastal blue | Blue | Green | Yellow | Red | Red-edge | NIR-1 | NIR-2 |
|---|---|---|---|---|---|---|---|---|
| **Coastal blue** | - | ns | ns | ** | ns | ns | ns | ns |
| **Blue** | **0.93** | - | ns | ns | ns | ns | ns | ns |
| **Green** | 0.20 | -0.10 | - | ns | ns | ns | ** | ns |
| **Yellow** | -0.94 | -0.90 | -0.06 | - | ns | ns | ns | ns |
| **Red** | -0.84 | -0.64 | -0.52 | 0.69 | - | ns | ns | ns |
| **Red-edge** | -0.39 | -0.65 | **0.81** | 0.40 | -0.15 | - | ns | ** |
| **NIR-1** | -0.02 | -0.33 | **0.97** | 0.18 | -0.41 | **0.94** | - | * |
| **NIR-2** | -0.10 | -0.44 | **0.94** | 0.22 | -0.31 | **0.97** | **0.99** | - |

551

**Table 8 -** Pairwise correlations among the eight bands of WorldView-3 (WV-3) imagery, computed from the reference sample trees of study area B. Correlation values are given in the lower triangle of the matrix, and the two-tailed probabilities are given in the upper (Correlations >0.75 in bold letters, ns: no significance; *p<0.01, **p<0.05).

| B Band | *Coastal blue* | *Blue* | *Green* | *Yellow* | *Red* | *Red-edge* | *NIR-1* | *NIR-2* |
|---|---|---|---|---|---|---|---|---|
| *Coastal blue* | - | ns | ns | ns | ** | ns | ns | ns |
| *Blue* | **0.96** | - | ns | ** | * | ns | ns | ** |
| *Green* | -0.09 | 0.02 | - | ns | ns | ns | ns | ns |
| *Yellow* | **0.89** | **0.98** | 0.15 | - | * | ns | ns | ns |
| *Red* | **0.92** | **0.97** | 0.12 | **0.98** | - | ns | ns | ns |
| *Red-edge* | -0.91 | -0.85 | 0.25 | -0.80 | -0.85 | - | * | * |
| *NIR-1* | -0.91 | -0.92 | 0.20 | -0.83 | -0.87 | **0.98** | - | * |
| *NIR-2* | -0.91 | -0.90 | 0.32 | -0.84 | -0.91 | **0.98** | **0.99** | - |

555

## 4.4 Spectral ANOVA test

In each plot, differences in spectral values between every single wavelength of sample trees were tested with one-way ANOVA. Results show significant differences among Yellow, Red, RE, NIR1 and NIR2 band in each plot study area A (Table 8). In B, results show significant differences in reflectance values between all bands in almost all plots, with the maximum of differences in RE, NIR1 and NIR2 bands (Table 10).

Referring to study area A, post-hoc tests (Tukey HSD, Mann-Whitney) emphasized that red spectral region was significantly different in the following plots comparison: $A_1/A_2$, $A_1/A_4$, $A_3/A_4$ (Table 9). The obtained spectral behavior of NIR1 and NIR2 revealed that such differences were statistically significant for a higher number of plots (Table 9).

**Table 9 -** Summary of normality, homoscedasticity tests and ANOVA statistics result of all grouped band reflectance value, among all A plots. Summary of post-hoc test for significant band comparison [ns: no significance; different letters indicate the different plots where single band reflectance values significantly differ (p < 0.05)].

| Band | Wavelength [nm] | Levene's test (p-value) | Shapiro-Wilk (W) | F | Welch test (F) | Kruskal Wallis (H) | Tukey HSD test (Q) | Mann-Whitney (U) |
|---|---|---|---|---|---|---|---|---|
| *C. blue* | 400-450 | 0.003 | 0.974* | | 1.57 | 7.80 | ns | |
| *Blue* | 450-510 | 0.335 | 0.971 | 1.00 | | | ns | |
| *Green* | 510-580 | 0.355 | 0.985 | 1.34 | | | ns | |
| *Yellow* | 585-625 | 0.713 | 0.981 | 4.82* | | | $A_3/A_4$ | |
| *Red* | 630-690 | 0.188 | 0.991 | 3.59* | | | $A_1/A_2$, $A_1/A_4$, $A_3/A_4$ | |
| *Red-edge* | 705-745 | 0.032 | 0.973* | | 45.2* | 89.50* | | $A_1/A_2$, $A_1/A_4$, $A_2/A_3$, $A_3/A_4$ |
| *NIR1* | 770-895 | 0.865 | 0.993 | 71.6* | | | $A_1/A_2$, $A_1/A_3$, $A_1/A_4$, $A_2/A_3$, $A_3/A_4$ | |

| Band | Wavelength (nm) | Levene's test (p-value) | Shapiro-Wilk (W) | F | Welch test (F) | Kruskal Wallis (H) | Tukey HSD test (Q) | Mann-Whitney (U) |
|---|---|---|---|---|---|---|---|---|
| *NIR2* | 860-1040 | 0.753 | 0.994 | 56.4* | | | $A_1/A_2$, $A_1/A_3$, $A_1/A_4$, $A_2/A_3$, $A_3/A_4$ | |

*marked value are where spectral signatures differ statistically for *p*-value <0.05

**Table 10.** Summary of normality, homoscedasticity tests and ANOVA statistics result of all grouped band reflectance value, among all B plots. Summary of post-hoc test for significant band comparison [ns: no significance; different letters indicate the different plots where single band reflectance values significantly differ (p < 0.05)].

| Band | Wavelength (nm) | Levene's test (p-value) | Shapiro-Wilk (W) | F | Welch test (F) | Kruskal Wallis (H) | Tukey HSD test (Q) | Mann-Whitney (U) |
|---|---|---|---|---|---|---|---|---|
| *C. blue* | 400-450 | 0.053 | 0.972 | 3.14* | | | $B_2/B_3$ | |
| *Blue* | 450-510 | 0.173 | 0.963 | 32.0* | | | $B_1/B_2$, $B_2/B_3$, $B_2/B_4$ | |
| *Green* | 510-580 | 0.015 | 0.975* | | 7.12* | 15.18* | | $B_1/B_4$, $B_3/B_4$ |
| *Yellow* | 585-625 | 0.174 | 0.942 | 49.8* | | | $B_1/B_2$, $B_2/B_3$, $B_1/B_4$, $B_1/B_3$ | |
| *Red* | 630-690 | 0.532 | 0.923 | 155.2* | | | $B_1/B_2$, $B_1/B_3$, $B_1/B_4$, $B_2/B_3$, $B_2/B_4$ | |
| *Red-edge* | 705-745 | 0.007 | 0.981* | | 168.0* | 93.02* | $B_1/B_2$, $B_1/B_4$, $B_2/B_3$, $B_2/B_4$, $B_3/B_4$ | |
| *NIR1* | 770-895 | 0.020 | 0.993* | | 267.4* | 88.77* | | $B_1/B_2$, $B_1/B_4$, $B_2/B_3$, $B_3/B_4$, |
| *NIR2* | 860-1040 | 0.000 | 0.985* | | 218.3* | 85.69* | | $B_1/B_2$, AC, $B_1/B_4$, $B_2/B_3$, $B_2/B_4$ |

*marked value are where spectral signature differ statistically for *p*-value <0.05

There was only one statistically significant differences between plots $A_3$:$A_4$ in the yellow wavelength value. In study area B, post-hoc tests showed a higher number of plot pairs that were statistically different in the whole spectrum region (Table 10), confirming the heterogeneous behavior of all olive trees between plots.

## 5. Discussion

The reliability of WV-3 data has been thoroughly tested and confirmed by the high overall accuracies of the obtained results, thanks to their high spectral, radiometric and spatial resolution. Due to the high

584    geometrical resolution of WV-3 imagery, it was possible to perform an overall accurate olive tree

585    crown extraction and derive VIs maps that cancel or diminish the effect of soil brightness as in cases

586    where vegetation is sparse and the pixels in the image are a combination of vegetation and soil

587    information  (Huete, 1988). In our proposed methodology, olive tree canopy boundaries extracted via

588    GEOBIA procedure, provided good results with an overall tree detection rate greater than 95% ($R^2$ =

589    0.98). Although several studies have reported the identification and extraction of TCA for other fruit

590    crop type with WV imagery (Anderson et al., 2018; Rahman et al., 2018; Robson et al., 2017), our

591    proposed semiautomatic procedure of detection and extraction of olive TCA provided a close to real

592    canopy shape boundary, if compared to the abovementioned works. Our findings showed that our

593    methodology allowed to correctly detect and extract very small olive trees with a TCA of 0.096 $m^2$

594    (corresponding to nine pixels).

595    Olive orchard mapping reaches a high overall accuracy with high kappa coefficient values in both

596    study areas (Table 5) especially when compared with other studies that used the same sensor, both in

597    the general classification of a scene as well as on the identification of individual objects (Han et al.,

598    2017; Johnson et al., 2017; Koenig and Gueguen, 2016; Majid et al., 2016; Srestasathiern and

599    Rakwatin, 2014; Ye et al., 2017). Nevertheless, as can be observed in the subplot details (figg. 8 and

600    9), our implemented procedure tends to loose portions of them or, depending on their shape, divides

601    them into two or more objects.

602    On the other hand, our results are in line with those reported in researches based on other types of

603    VHR images (Aguilar et al., 2013, 2016; Alrassi et al., 2016; Gaertner, 2017; Immitzer et al., 2012;

604    Kaszta et al., 2016; Kux and Souza, 2012; Shahi et al., 2017). The comparison of our findings with

605    those coming similar studies carried out in crops (Díaz-Varela et al., 2015; Karydas et al., 2017), but

606    with images acquired by unmanned aerial vehicles (UAVs) and therefore with a higher geometric

607    resolution, gives the idea of the very satisfying results we achieved and the promising potential in

608    reaching the obtained high accuracy applying our methodology to other crops. By the way, according

609    to Wolf (né Straub) and Heipke, 2007, the results on individual tree crown delineation are difficult to

610    standardize and to compare among different researches. This, because of significant differences in

611    study sites, scene characteristics, data sets (spatial and spectral resolutions) and tree types. The shadow

612    effect may probably explain the worst detection rate reported for study area A, coupled with smaller

613    size of olive tree.

614    The effect of shadow has been found to be dependent on the sun azimuth angle in relation to the

615    satellite position at the time of imaging (Leckie et al., 2005) and when this occur vegetation

616    reflectance results disturbed, although satellite over- pass times are programmed to minimize on

617    shadow effect (Chemura et al., 2015). The effect of manual on-screen digitizing of reference data

618    should also be considered when performing the accuracy assessment, and expert knowledge must be

619    provided.

620    The comparison of the spectral reflectance data with the results offered by the pan-sharpened WV-3

621    eight bands orthoimage showed a relatively good agreement between VIs and spectral responses of

622    vegetation and soil targets. Previous studies have already discussed the use of four newly available

623    WV family spectral bands (coastal, green, yellow, red edge) for the classification of the tree species

624    (Immitzer et al., 2012; Pu and Landry, 2012). In our research, it was found that the major differences

625    in spectral behavior, among different plots of the same olive orchard, are mainly due to the component

626    of the red-infrared regions of the EM spectrum, where the RE becomes important in assessing the state

627    of general vigor. It should be pointed out that as we used Digital Numbers (DN) rather than calibrated

628    reflectance values, our results are more qualitative than quantitative, affecting the raw indices results

629    by some modifications in the traditional scale ranges, however ensuring a good description of the

630    vegetation status. As suggested by Candiago et al (2015) VIs were based on DNs due to the absence of

631    ground measurements needed for ground reflectance calibration.

632    VIs results faithfully reflects the different olive orchard vigor conditions among the two-study areas

633    and the different plots. In fact, as confirmed by owners of study area A, over the years, olive orchard

634    have suffered various diseases (olive peacock spot, olive knot disease, olive thrips) that have not

635    allowed an optimal development. Moreover, the soil, mainly clayey and compact, is difficult to work

636    especially in spring and summer seasons, with consequences on plants stress condition. Indeed, a state

637    of better vigor was found in all plots of study area B so that VIs were able to capture the spatial

638    variability of olive tree, deriving from different management practices, such as fertilization or pruning,

639    and the optimal soil condition. Increases in VIs' values in red and NIR bands lead to an increase of

640    canopy cover and LAI, a typical characteristic of green vegetation related to the chlorophyll content

641    and the leaf parenchyma (Horler et al., 1983a; Horler et al., 1983b). VIs based on VIS and NIR

642    reflectance values have been developed taking advantage of the contrast in reflectance behavior

643    between the red and NIR portions of the EM spectrum (Sripada et al., 2008).

644    In this paper, we reported that using reflectance data from WV-3 imagery, could reliably deliver VIs

645    able to detect healthy or unhealthy portions of a cultivated olive orchard. The use of olive tree canopy

646    spectra for vigor assessment mostly depends on the close relationship between nitrogen (N) and

647    chlorophylls in the cell metabolism (Shiratsuchi et al., 2011). The Red band-based VIs like NDVI and

648    NDRE are the most common indices in N status estimation. However, the red band can be easily

649    influenced by soil background reflectance at early growth stages when vegetation coverage is small, as

650    it is in study area A. In our research, the NDRE index significantly improved the estimation results

651    compared to NDVI (Table 6). This is because the RE reflectance is highly correlated with chlorophyll

652    content (Cho and Skidmore, 2006; Clevers et al., 2002), and is responsive to variation in LAI or

653    biomass (Gnyp et al., 2014; Haboudane et al., 2008).

654    In addition, NDRE is insensitive to background effects (Zarco-Tejada et al., 2004). Our results also

655    confirmed the findings of a research on summer maize by Li et al. (2014), who found that the NDRE

656    improved the plant N concentration estimations. The main function of VIs, other than NDVI, also

657    relies on the possibility to compensate for the effects of disturbing factors such as crop type, LAI, or

658    canopy biomass (Bouman, 1995). MCARI2 also succeeded in minimize soil background and LAI

659    variation in olive trees, as found also by (Zarco-Tejada et al., 2004) in providing predictive

660    relationships for chlorophyll concentration estimation with narrow-band imagery in open tree canopy

661    orchards. More in-depth, statistical analysis has shown that the first five bands do not provide

662    additional information under these conditions, reporting no significant difference in all plots and that

663    VIs are mainly influenced by RE, NIR1, and NIR2 values.

664    RE and the two NIR bands explained the most variability, therefore are the main responsible of

665    significant differences in VIs values in the statistical analysis and on which, therefore, depends most

666    of the variability of the vegetative state of the olive trees. This was also observed in wheat LAI

667    estimation by Herrmann et al. (2011). WV-3 band properties, along with indices that are based on

668    reflectance in the RE spectrum region, provided  to be very sensitive to olive canopy chlorophyll and

669    N status due to the rapid change in leaf reflectance caused by the strong absorption by pigments in the

670    red spectrum and leaf scattering in the NIR spectrum (Hatfield et al., 2008; Hatfield and Prueger,

671    2010; Nguy-Robertson et al., 2012). This analysis shows the importance of incorporating the RE

672    channel, and two NIR bands particularly in terms of capturing the differences between the decrease

673    and increase in the LAI in an open canopy tree cover. Results show that WV-3 data could improve

674    classification and vegetation health monitoring, coupled with VIs computation, over WV-2 and other

675    satellite sensor as Landsat 8, QuickBird, Pleiades and SPOT (Han et al., 2017; Immitzer et al., 2012;

676    Majid et al., 2016). The additional VNIR bands (including the RE and yellow bands) at fine pixel scale

677    provide a significant improvement over the other satellite platform sensed image. Furthermore, with

678    the additional shortwave infra-red (SWIR) information included in the VW -3 image, the data set

679    could performs as well as a full hyperspectral sensor (Han et al., 2017).

680    This study demonstrated that high spatial resolution satellite data makes olive orchard precision

681    monitoring possible, and in further studies, radiometric ground truth data can be used to calibrate and

682    map the time series of olive growth condition, filling the limits of this method, applied to relatively

683    large, homogeneous, single-layer agricultural or forest ecosystems (Maselli et al. 2014). To address

684    PA applications to spatially fragmented and multi-layer agricultural ecosystems that are common in

685    southern Mediterranean rural areas, there is the need to face with further challenges. One of the most

686    important concerns the spatial distribution and size of most of the European agricultural olive groves

687    systems, as well as vineyards an any tree plantations, which are generally far below the resolution of

688    widely used remote sensed imagery (Landsat or MODIS). These ecosystems are found over irregular

689    terrain and occupy small unit areas (around 0.1–0.5 ha) (Maselli et al., 2012) in many agricultural

690    situations. Among the possible solutions implemented by research, one of the most common solutions

691    that are being adopted could be the integration of high spatial resolution satellite data, such as WV-3

692    data, with those acquired through UAVs with higher spatial resolution. This is confirmed by recent

693    experimental studies carried out in several crop systems (Palchowdhuri et al., 2018), which indicate

694    that such integration leads to a clear improvement in crop management. The VW series of satellites

695    (2009) provided further enhancements to spectral monitoring with 8 multi-spectral bands at very high

696     spatial resolutions in addition to 8 SWIR bands. Despite sensor capabilities, the potential of WV-3

697     imagery for PA purposes has yet to be fully realized due to prohibitively expensive image acquisition

698     costs, even in the context of continuous monitoring. This highlights the gap currently existing between

699     expensive commercial and free data systems in terms of their potential applications, particularly

700     evident in the case of PA (Houborg et al., 2015). To this end the pair of new Sentinel-2 satellites (S-

701     2A, S-2B), will bridge this gap by delivering narrower band multispectral data (including 2 narrow

702     bands in RE) at 10 m resolutions with a 5 days revisit frequency. Despite of a spatial resolution lower

703     than WW-3, this will give the opportunity to significantly improve the ability to monitor the state and

704     function of worldwide vegetation, through enhanced definition of the RE coupled with crop scouting.

705     Therefore, agricultural systems could be monitored throughout the growing season and a reliable

706     decision support system, based on RS information, could be achievable (Basso et al., 2004; Wojtowicz

707     et al., 2016).

708

## 6. Conclusions

710     The present paper showed the main findings and the potentialities of a semiautomatic process

711     workflow implemented on WV-3 imagery and aimed at obtaining VIs at tree detail in olive crops,

712     without any ground radiometric measure. The results from this study confirm the potential of high

713     resolution WV-3 imagery for accurately derive olive tree crown boundaries across two different olive

714     orchards in Calabria region, southern Italy. Tree crown detection and extraction were optimized, thus

715     achieving high geometric accuracy obtaining a close to real canopy shape boundary.

716     VIs maps revealed more contrast and more properties than those resulting visually evident from true

717     and false colors image analysis, while the spatial distribution of NDVI, MSAVI2, NDRE, MCARI2,

718     NDVI2 already showed significant pattern, where the zones with negative behavior were well

719     recognizable. Due to the heterogeneous extension and composition characterizing agricultural

720     ecosystems in southern Mediterranean areas, visual interpretation and tree detection can be

721     significantly improved by the data enrichment provided through the sharpening of WV-3 multispectral

722     bands with the panchromatic one.

723     Statistical analyses showed that the major differences in spectral behavior, over different plots of the

724     two investigated olive orchards, are mainly due to the component of the red-infrared regions of the

725     EM spectrum, where the RE becomes important in assessing the state of vegetation vigor.

726     The proposed classification method is very promising, since it provides an operational processing

727     chain for mapping and monitoring olive orchards at tree detail, thus allowing to identify healthy or

728     unhealthy portions of the analyzed crop. On the other hand, our study confirms that GEOBIA

729     classification and single tree crown extraction benefit from suitable conditions of olive crops

730     characterized by regular planting patterns with minimum overlap. Additional RS technologies, such as

731     a low-altitude remote sensing based on UAVs, may be adopted to overcome these limitations. By the

732     way, satellite imagery has proven to be cost-effective compared to UAV imagery in terms of area

733     coverage, processing and pre-processing need for geometric and radiometric calibrations, spectral

734     information, and less costs in collecting reference data sampling.

735     This study provided a novel contribution in exploring the reliability of WV-3 multispectral imagery in

736     PA applications. The proposed methodology, when applied to an operational field, has proven to be

737     quick and cost-effective. Moreover, our research offers an original and innovative contribution

738     increasing the knowledge in olive crop management and monitoring, at tree detail, from VHR satellite

739     imagery.

740     At the present stage of our research, our findings and conclusions could be extended to other cases

741     only after comparison with the results of other studies concerning olive orchard conditions similar to

742     those here investigated. Further studies may investigate how to take advantage from high spatial

743     resolution satellite imagery, as that provided by WV-3 sensor, by linking it to an adequate ground truth

744     data collection.

745

751

752   **7. References**

Aguilar, M. a, Saldaña, M.M., Aguilar, F.J., 2013. GeoEye-1 and WorldView-2 pan- sharpened imagery for object-based classification in urban environments. Int. J. Remote Sens. 34, 2583–2606. doi:10.1080/01431161.2012.747018

Aguilar, M.A., Aguilar, F.J., García Lorca, A., Guirado, E., Betlej, M., Cichon, P., Nemmaoui, A., Vallario, A., Parente, C., 2016. Assessment of multiresolution segmentation for extracting greenhouses from WorldView-2 imagery. Int. Arch. Photogramm. Remote Sens. Spat. Inf. Sci. - ISPRS Arch. 41, 145–152. doi:10.5194/isprsarchives-XLI-B7-145-2016

Alrassi, F., Salim, E., Nina, A., Alwi, L., Danoedoro, P., Kamal, M., 2016. GEOBIA for Land Use Mapping Using Worldview2 Image in Bengkak Village Coastal, Banyuwangi Regency, East Java. IOP Conf. Ser. Earth Environ. Sci. 47. doi:10.1088/1755-1315/47/1/012009

Anderson, N.T., Underwood, J.P., Rahman, M.M., Robson, A., Walsh, K.B., 2018. Estimation of fruit load in mango orchards: tree sampling considerations and use of machine vision and satellite imagery. Precis. Agric. 1–17. doi:10.1007/s11119-018-9614-1

Balthazar, V., Vanacker, V., Lambin, E.F., 2012. Evaluation and parameterization of ATCOR3 topographic correction method for forest cover mapping in mountain areas. Int. J. Appl. Earth Obs. Geoinf. 18, 436–450. doi:10.1016/j.jag.2012.03.010

Barnes, E., Clarke, T., Richards, S., Colaizzi, P., Haberland, J., Kostrzewski, M., Waller, P., Choi, C., Riley, E., Thompson, T., Lascano, R.J., Li, H., Moran, M., 2000. Coincident detection of crop water stress, nitrogen status and canopy density using ground-based multispectral data, in: Fifth International Conference on Precision Agriculture.

Basso, B., Cammarano, D., De Vita, P., 2004. Remotely sensed vegetation indices: Theory and applications for crop management. Ital. J. Agrometeorol. 53, 36–53.

Bausch, W.C., Khosla, R., 2010. QuickBird satellite versus ground-based multi-spectral data for estimating nitrogen status of irrigated maize. Precis. Agric. 11, 274–290. doi:10.1007/s11119-009-9133-1

Benalia, S., Bernardi, B., Blasco, J., Fazari, A., Zimbalatti, G., 2017. Assessment of the Ripening of Olives Using Computer Vision. Chem. Eng. Trans. 58, 355–360. doi:10.3303/CET1758060

Blaschke, T., 2010. Object based image analysis for remote sensing. ISPRS J. Photogramm. Remote Sens. 65, 2–16. doi:10.1016/j.isprsjprs.2009.06.004

Blaschke, T., Hay, G.J., Kelly, M., Lang, S., Hofmann, P., Addink, E., Queiroz Feitosa, R., van der Meer, F., van der Werff, H., van Coillie, F., Tiede, D., 2014. Geographic Object-Based Image Analysis – Towards a new paradigm. ISPRS J. Photogramm. Remote Sens. 87, 180–191. doi:10.1016/j.isprsjprs.2013.09.014

Bouman, B.A.M., 1995. Crop modelling and remote sensing for yield prediction. Netherl. J. Agric. Sci. 43, 143–161.

Broge, N.H., Leblanc, E., 2001. Comparing prediction power and stability of broadband and hyperspectral vegetation indices for estimation of green leaf area index and canopy chlorophyll density. Remote Sens. Environ. 76, 156–172. doi:10.1016/S0034-4257(00)00197-8

Calderón, R., Navas-Cortés, J.A., Lucena, C., Zarco-Tejada, P.J., 2013. High-resolution airborne hyperspectral and thermal imagery for early detection of Verticillium wilt of olive using fluorescence, temperature and narrow-band spectral indices. Remote Sens. Environ. 139, 231–245. doi:10.1016/j.rse.2013.07.031

Calderón, R., Navas-Cortés, J.A., Zarco-Tejada, P.J., 2015. Early detection and quantification of Verticillium Wilt in olive using hyperspectral and thermal imagery over large areas. Remote Sens. 7, 5584–5610. doi:10.3390/rs70505584

Calvão, T., Palmeirim, J.M., 2004. Mapping Mediterranean scrub with satellite imagery: biomass estimation and spectral behaviour. Int. J. Remote Sens. 25, 3113–3126. doi:10.1080/01431160310001654978

Cammarano, D., Fitzgerald, G.J., Casa, R., Basso, B., 2014. Assessing the robustness of vegetation indices to estimate wheat N in mediterranean environments. Remote Sens. 6, 2827–2844. doi:10.3390/rs6042827

Chemura, A., van Duren, I., van Leeuwen, L.M., 2015. Determination of the age of oil palm from crown projection area detected from WorldView-2 multispectral remote sensing data: The case of Ejisu-Juaben district, Ghana. ISPRS J. Photogramm. Remote Sens. 100, 118–127. doi:10.1016/j.isprsjprs.2014.07.013

Chepkochei, L., 2011. Object-oriented image classification of individual trees using Erdas Imagine Objective: Case study of Wanjohi area, Lake Naivasha Basin, Kenya. Proceedings, Kenya Geotherm. Conf.

804 Cho, M.A., Skidmore, A.K., 2006. A new technique for extracting the red edge position from hyperspectral data:
805     The linear extrapolation method. Remote Sens. Environ. 101, 181–193. doi:10.1016/j.rse.2005.12.011

806 Chuang, Y.C.M., Shiu, Y.S., 2016. A comparative analysis of machine learning with worldview-2 pan-
807     sharpened imagery for tea crop mapping. Sensors (Switzerland) 16. doi:10.3390/s16050594

808 Clevers, J.G.P.W., De Jong, S.M., Epema, G.F., Van Der Meer, F.D., Bakker, W.H., Skidmore, A.K., Scholte,
809     K.H., 2002. Derivation of the red edge index using the MERIS standard band setting. Int. J. Remote Sens.
810     23, 3169–3184. doi:10.1080/01431160110104647

811 Congalton, R.G., 1991. A review of assessing the accuracy of classifications of remotely sensed data. Remote
812     Sens. Environ. 37, 35–46. doi:10.1016/0034-4257(91)90048-B

813 Congalton, R.G., Green, K., 2008. Assessing the Accuracy of Remotely Sensed Data: Principles and Practices,
814     Second Edition, Second Edi. ed. CRC Press.

815 Dahiya, S., Garg, P.K., Jat, M.K., 2013. A comparative study of various pixel-based image fusion techniques as
816     applied to an urban environment. Int. J. Image Data Fusion 4, 197–213.
817     doi:10.1080/19479832.2013.778335

818 Daughtry, C., 2000. Estimating Corn Leaf Chlorophyll Concentration from Leaf and Canopy Reflectance.
819     Remote Sens. Environ. 74, 229–239. doi:10.1016/S0034-4257(00)00113-9

820 de Graaff, J., Eppink, L.A.A.., 1999. Olive oil production and soil conservation in southern Spain, in relation to
821     EU subsidy policies. Land use policy 16, 259–267. doi:10.1016/S0264-8377(99)00022-8

822 Di Fazio, S., Modica, G., 2018. Historic Rural Landscapes: Sustainable Planning Strategies and Action Criteria.
823     The Italian Experience in the Global and European Context. Sustainability 10, 3834.
824     doi:10.3390/su10113834

825 Díaz-Varela, R., de la Rosa, R., León, L., Zarco-Tejada, P., 2015. High-Resolution Airborne UAV Imagery to
826     Assess Olive Tree Crown Parameters Using 3D Photo Reconstruction: Application in Breeding Trials.
827     Remote Sens. 7, 4213–4232. doi:10.3390/rs70404213

828 Eckert, S., 2012. Improved Forest Biomass and Carbon Estimations Using Texture Measures from WorldView-2
829     Satellite Data. Remote Sens. 4, 810–829. doi:10.3390/rs4040810

830 Eitel, J.U.H., Long, D.S., Gessler, P.E., Smith, A.M.S., 2007. Using in-situ measurements to evaluate the new
831     RapidEye ™ satellite series for prediction of wheat nitrogen status. Int. J. Remote Sens. 28, 4183–4190.
832     doi:10.1080/01431160701422213

833 Erikson, M., 2004. Species classification of individually segmented tree crowns in high-resolution aerial images
834     using radiometric and morphologic image measures. Remote Sens. Environ. 91, 469–477.
835     doi:10.1016/j.rse.2004.04.006

836 Fitzgerald, G.J., 2010. Characterizing vegetation indices derived from active and passive sensors. Int. J. Remote
837     Sens. 31, 4335–4348. doi:10.1080/01431160903258217

838 Foxhall, L., 2007. Olive Cultivation in Ancient Greece: Seeking the Ancient Economy. Oxford University Press,
839     New York, NY, USA.

840 Gaertner, J., 2017. Vegetation classification of Coffea on Hawaii Island using WorldView-2 satellite imagery. J.
841     Appl. Remote Sens. 11, 1. doi:10.1117/1.JRS.11.046005

842 Gnyp, M.L., Miao, Y., Yuan, F., Ustin, S.L., Yu, K., Yao, Y., Huang, S., Bareth, G., 2014. Hyperspectral canopy
843     sensing of paddy rice aboveground biomass at different growth stages. F. Crop. Res. 155, 42–55.
844     doi:10.1016/j.fcr.2013.09.023

845 Goutte, C., Gaussier, E., 2005. A Probabilistic Interpretation of Precision, Recall and F-Score, with Implication
846     for Evaluation. pp. 345–359. doi:10.1007/978-3-540-31865-1_25

847 Haboudane, D., Miller, J.R., Pattey, E., Zarco-Tejada, P.J., Strachan, I.B., 2004. Hyperspectral vegetation
848     indices and novel algorithms for predicting green LAI of crop canopies: Modeling and validation in the
849     context of precision agriculture. Remote Sens. Environ. 90, 337–352. doi:10.1016/j.rse.2003.12.013

850 Haboudane, D., Tremblay, N., Miller, J.R., Vigneault, P., 2008. Remote Estimation of Crop Chlorophyll Content
851     Using Spectral Indices Derived From Hyperspectral Data. IEEE Trans. Geosci. Remote Sens. 46, 423–437.
852     doi:10.1109/TGRS.2007.904836

853 Han, J., Wei, C., Chen, Y., Liu, W., Song, P., Zhang, D., Wang, A., Song, X., Wang, X., Huang, J., 2017.

Mapping Above-Ground Biomass of Winter Oilseed Rape Using High Spatial Resolution Satellite Data at Parcel Scale under Waterlogging Conditions. Remote Sens. 9, 238. doi:10.3390/rs9030238

Hatfield, J.L., Gitelson, A.A., Schepers, J., Walthall, C.L., 2008. Application of Spectral Remote Sensing for Agronomic Decisions. Agron. J. S-117-S-131. doi:10.2134/agronj2006.0370c

Hatfield, J.L., Prueger, J.H., 2010. Value of Using Different Vegetative Indices to Quantify Agricultural Crop Characteristics at Different Growth Stages under Varying Management Practices. Remote Sens. 2, 562–578. doi:10.3390/rs2020562

Herrmann, I., Pimstein, A., Carnieli, A., Cohen, Y., Alchanatis, V., Bonfil, D.J., 2011. LAI assessment of wheat and potato crops by VEN µ S and Sentinel-2 bands. Remote Sens. Environ. 115, 2141–2151. doi:10.1016/j.rse.2011.04.018

Horler, D. N. H., Dockray, M., Barber, J., 1983. The red edge of plant leaf reflectance. Int. J. Remote Sens. 4, 273–288. doi:10.1080/01431168308948546

Horler, D.N.H., Dockray, M., Barber, J., Barringer, A.R., 1983. Red edge measurements for remotely sensing plant chlorophyll content. Adv. Sp. Res. 3, 273–277. doi:10.1016/0273-1177(83)90130-8

Houborg, R., McCabe, M., Cescatti, A., Gao, F., Schull, M., Gitelson, A., 2015. Joint leaf chlorophyll content and leaf area index retrieval from Landsat data using a regularized model inversion system (REGFLEC). Remote Sens. Environ. 159, 203–221. doi:10.1016/j.rse.2014.12.008

Huete, A.R., 1988. A Soil-Adjusted Vegetation Index ( SAVI ). Remote Sens. Environ. 309, 295–309. doi:10.1016/0034-4257(88)90106-X

Hunt, E.R., Doraiswamy, P.C., McMurtrey, J.E., Daughtry, C.S.T., Perry, E.M., Akhmedov, B., 2013. A visible band index for remote sensing leaf chlorophyll content at the canopy scale. Int. J. Appl. Earth Obs. Geoinf. 21, 103–112. doi:10.1016/j.jag.2012.07.020

Hunt, E.R., Doraiswamy, P.C., McMurtrey, J.E., Daughtry, C.S.T., Perry, E.M., Akhmedov, B., 2012. A visible band index for remote sensing leaf chlorophyll content at the Canopy scale. Int. J. Appl. Earth Obs. Geoinf. 21, 103–112. doi:10.1016/j.jag.2012.07.020

Immitzer, M., Atzberger, C., Koukal, T., 2012. Tree Species Classification with Random Forest Using Very High Spatial Resolution 8-Band WorldView-2 Satellite Data. Remote Sens. 4, 2661–2693. doi:10.3390/rs4092661

International Olive Council, 2018. World Olive Oil Figures [WWW Document]. URL http://www.internationaloliveoil.org/estaticos/view/131-world-olive-oil-figures (accessed 10.30.18).

ISMEA, 2018. Piano di settore Olivicolo-oleario. La produzione italiana di olio di oliva. Stime della campagna produttiva 2017/18. Rome, Italy.

Johnson, K.E., Staff, R., Scientist, D., 2017. WorldView-3 Swir land use-land cover mineral classification: Cuprite, NEVADA, in: Observing a Changing Earth; Science for Decisions— Monitoring, Assessment, and Projection. Sioux Falls, SD.

Jolliffe, I.T., 2002. Principal Component Analysis. Second Edition. Springer Ser. Stat. 98, 487. doi:10.1007/b98835

Karydas, C., Gewehr, S., Iatrou, M., Iatrou, G., Mourelatos, S., 2017. Olive Plantation Mapping on a Sub-Tree Scale with Object-Based Image Analysis of Multispectral UAV Data; Operational Potential in Tree Stress Monitoring. J. Imaging 3, 57. doi:10.3390/jimaging3040057

Kaszta, Z., Van De Kerchove, R., Ramoelo, A., Cho, M.A., Madonsela, S., Mathieu, R., Wolff, E., 2016. Seasonal separation of African savanna components using WorldView-2 imagery: A comparison of pixeland object-based approaches and selected classification algorithms. Remote Sens. 8. doi:10.3390/rs8090763

Koc-San, D., Selim, S., Aslan, N., San, B.T., 2018. Automatic citrus tree extraction from UAV images and digital surface models using circular Hough transform. Comput. Electron. Agric. 150, 289–301. doi:10.1016/j.compag.2018.05.001

Koenig, J., Gueguen, L., 2016. A comparison of land use land cover classification using superspectral WorldView-3 vs hyperspectral imagery, in: 2016 8th Workshop on Hyperspectral Image and Signal Processing: Evolution in Remote Sensing (WHISPERS). IEEE, pp. 1–5. doi:10.1109/WHISPERS.2016.8071721

905 Kumar, M., Monteith, J.L., 1981. Remote sensing of crop growth, in: Smith, H. (Ed.), Plants and the Daylight
906    Spectrum. Academic Press, London, pp. 133–144.

907 Kux, H.J.H., Souza, U.D. V., 2012. Object-Based Image Analysis of Worldview-2 Satellite Data for the
908    Classification of Mangrove Areas in the City of São Luís, Maranhão State, Brazil. ISPRS Ann.
909    Photogramm. Remote Sens. Spat. Inf. Sci. I–4, 95–100. doi:10.5194/isprsannals-I-4-95-2012

910 Larsen, M., Eriksson, M., Descombes, X., Perrin, G., Brandtberg, T., Gougeon, F.A., 2011. Comparison of six
911    individual tree crown detection algorithms evaluated under varying forest conditions. Int. J. Remote Sens.
912    32, 5827–5852. doi:10.1080/01431161.2010.507790

913 Leckie, D.G., Gougeon, F.A., Tinis, S., Nelson, T., Burnett, C.N., Paradine, D., 2005. Automated tree
914    recognition in old growth conifer stands with high resolution digital imagery. Remote Sens. Environ. 94,
915    311–326. doi:10.1016/j.rse.2004.10.011

916 Li, F., Miao, Y., Feng, G., Yuan, F., Yue, S., Gao, X., Liu, Y., Liu, B., Ustin, S.L., Chen, X., 2014. Improving
917    estimation of summer maize nitrogen status with red edge-based spectral vegetation indices. F. Crop. Res.
918    157, 111–123. doi:10.1016/j.fcr.2013.12.018

919 Li, W., Guo, Q., Jakubowski, M.K., Kelly, M., 2012. A New Method for Segmenting Individual Trees from the
920    Lidar Point Cloud. Photogramm. Eng. Remote Sens. 78, 75–84. doi:10.14358/PERS.78.1.75

921 Loumou, A., Giourga, C., 2003. Olive groves: "The life and identity of the Mediterranean''." Agric. Human
922    Values 20, 87–95. doi:10.1023/A:1022444005336

923 Lu, X., Guo, Q., Li, W., Flanagan, J., 2014. A bottom-up approach to segment individual deciduous trees using
924    leaf-off lidar point cloud data. ISPRS J. Photogramm. Remote Sens. 94, 1–12.
925    doi:10.1016/j.isprsjprs.2014.03.014

926 Main, R., Cho, M.A., Mathieu, R., O'Kennedy, M.M., Ramoelo, A., Koch, S., 2011. An investigation into robust
927    spectral indices for leaf chlorophyll estimation. ISPRS J. Photogramm. Remote Sens. 66, 751–761.
928    doi:10.1016/j.isprsjprs.2011.08.001

929 Majid, I.A., Latif, Z.A., Adnan, N.A., 2016. Tree Species Classification Using Worldview-3 Data.

930 Maselli, F., Chiesi, M., Brilli, L., Moriondo, M., 2012. Simulation of olive fruit yield in Tuscany through the
931    integration of remote sensing and ground data. Ecol. Modell. 244, 1–12.
932    doi:10.1016/j.ecolmodel.2012.06.028

933 Maselli, F., Papale, D., Chiesi, M., Matteucci, G., Angeli, L., Raschi, A., Seufert, G., 2014. Operational
934    monitoring of daily evapotranspiration by the combination of MODIS NDVI and ground meteorological
935    data: Application and evaluation in Central Italy. Remote Sens. Environ. 152, 279–290.
936    doi:10.1016/j.rse.2014.06.021

937 Moder, K., 2010. Alternatives to F-Test in One Way ANOVA in case of heterogeneity ofvariances (a simulation
938    study). Psychol. Test Assess. Model. 52, 343–353.

939 Modica, G., Pollino, M., Solano, F., 2019. Sentinel-2 Imagery for Mapping Cork Oak (Quercus suber L.)
940    Distribution in Calabria (Italy): Capabilities and Quantitative Estimation, in: Calabrò, F., Della Spina, L.,
941    Bevilacqua, C. (Eds.), New Metropolitan Perspectives. ISHT 2018. Smart Innovation, Systems and
942    Technologies. Springer, Cham, pp. 60–67. doi:10.1007/978-3-319-92099-3_8

943 Mutanga, O., Adam, E., Adjorlolo, C., Abdel-Rahman, E.M., 2015. Evaluating the robustness of models
944    developed from field spectral data in predicting African grass foliar nitrogen concentration using
945    WorldView-2 image as an independent test dataset. Int. J. Appl. Earth Obs. Geoinf. 34, 178–187.
946    doi:10.1016/j.jag.2014.08.008

947 Nebikera, S., Nebikera, S., Annena, A., Scherrerb, M., Oeschc, D., 2008. A Light-weight Multispectral Sensor
948    for Micro UAV - Opportunities for very high resolution airborne remote sensing. Int. Arch. Photogramm.
949    Remote Sens. Spat. Inf. Sci. 1193–1200.

950 Ng, W.-T., Rima, P., Einzmann, K., Immitzer, M., Atzberger, C., Eckert, S., 2017. Assessing the Potential of
951    Sentinel-2 and Pléiades Data for the Detection of Prosopis and Vachellia spp. in Kenya. Remote Sens. 9,
952    74. doi:10.3390/rs9010074

953 Nguy-Robertson, A., Gitelson, A., Peng, Y., Vina, A., Arkebauer, T., Rundquist, D., 2012. Green leaf area index
954    estimation in maize and soybean: combining vegetation indices to achieve maximal sensitivity. Agron. J.
955    1336–1347. doi:10.2134/agronj2012.0065

956 Ok, A.O., Senaras, C., Yuksel, B., 2013. Automated detection of arbitrarily shaped buildings in complex
957     environments from monocular VHR optical satellite imagery. IEEE Trans. Geosci. Remote Sens. 51,
958     1701–1717. doi:10.1109/TGRS.2012.2207123

959 Ortega-Farías, S., Ortega-Salazar, S., Poblete, T., Kilic, A., Allen, R., Poblete-Echeverría, C., Ahumada-
960     Orellana, L., Zuñiga, M., Sepúlveda, D., 2016. Estimation of Energy Balance Components over a Drip-
961     Irrigated Olive Orchard Using Thermal and Multispectral Cameras Placed on a Helicopter-Based
962     Unmanned Aerial Vehicle (UAV). Remote Sens. 8, 638. doi:10.3390/rs8080638

963 Padwick, C., Deskevich, M., Pacifici, F., Smallwood, S., 2010. Worldview-2 pan-sharpening, in: ASPRS 2010
964     Annual Conference. San Diego, California.

965 Palchowdhuri, Y., Valcarce-Diñeiro, R., King, P., Sanabria-Soto, M., 2018. Classification of multi-temporal
966     spectral indices for crop type mapping: A case study in Coalville, UK. J. Agric. Sci. 156, 24–36.
967     doi:10.1017/S0021859617000879

968 Pauly, K., 2014. Applying Conventional Vegetation Vigor Indices To UAS-Derived Orthomosaics: Issues And
969     Considerations. Ispa.

970 Petrucci, O., Polemio, M., Pasqua, A.A., 2009. Analysis of damaging hydrogeological events: The case of the
971     calabria region (Southern Italy). Environ. Manage. 43, 483–495. doi:10.1007/s00267-008-9234-z

972 Pettorelli, N., 2013. The Normalized Difference Vegetation Index. Oxford University Press, Oxford, UK.

973 Prince, S.D., 1990. High temporal fraquency remote sensing of primary productionusing NOAA AVHRR, in:
974     Applications of Remote Sensing in Agriculture. Elsevier, pp. 169–183. doi:10.1016/B978-0-408-04767-
975     8.50016-5

976 Pu, R., Landry, S., 2012. A comparative analysis of high spatial resolution IKONOS and WorldView-2 imagery
977     for mapping urban tree species. Remote Sens. Environ. 124, 516–533. doi:10.1016/j.rse.2012.06.011

978 Qi, J., Chehbouni, A., Huete, A.R., Kerr, Y.H., Sorooshian, S., 1994. A modified soil adjusted vegetation index.
979     Remote Sens. Environ. 48, 119–126. doi:10.1016/0034-4257(94)90134-1

980 R Core Team, 2017. R: A language and environment for statistical computing.

981 Rahman, M., Robson, A., Bristow, M., Rahman, M.M., Robson, A., Bristow, M., 2018. Exploring the Potential
982     of High Resolution WorldView-3 Imagery for Estimating Yield of Mango. Remote Sens. 10, 1866.
983     doi:10.3390/rs10121866

984 Richards, J.A., Jia, X., 2006. Remote Sensing Digital Image Analysis. An introduction. Springer-Verlag,
985     Berlin/Heidelberg. doi:10.1007/3-540-29711-1

986 Richter, R., 1998. Correction of satellite imagery over mountainous terrain. Appl. Opt. 37, 4004–15.

987 Richter, R., 1997. Correction of atmospheric and topographic effects for high spatial resolution satellite imagery.
988     Int. J. Remote Sens. 18, 1099–1111. doi:10.1080/014311697218593

989 Richter, R., Kellenberger, T., Kaufmann, H., 2009. Comparison of Topographic Correction Methods. Remote
990     Sens. 1, 184–196. doi:10.3390/rs1030184

991 Roberts, D., Roth, K., Perroy, R., 2011. Hyperspectral Vegetation Indices, in: Hyperspectral Remote Sensing of
992     Vegetation. CRC Press, pp. 309–328. doi:10.1201/b11222-20

993 Robson, A., Rahman, M., Muir, J., Robson, A., Rahman, M.M., Muir, J., 2017. Using Worldview Satellite
994     Imagery to Map Yield in Avocado (Persea americana): A Case Study in Bundaberg, Australia. Remote
995     Sens. 9, 1223. doi:10.3390/rs9121223

996 Rouse, J.W., Haas, R.H., Schell, J.A., Deering, D.W., 1974. Monitoring Vegetation Systems in the Great Plains
997     with Erts, in: Stanley Freden, C., Mercanti, Enrico P., Becker, M.A. (Eds.), Third Earth Resources
998     Technology Satellite 1 Symposium. NASA, Washington, D.C., USA.

999 Sepulcre-Cantò, G., Zarco-Tejada, P.J., Sobrino, J. a., Jimenez-Munoz, J.C., Villalobos, E., 2005. Spatial
1000     variability of crop water stress in an olive grove with high-spatial thermal remote sensing imagery. Precis.
1001     Agric. '05 267–272.

1002 Shahi, K., Shafri, H.Z.M., Hamedianfar, A., 2017. Road condition assessment by OBIA and feature selection
1003     techniques using very high-resolution WorldView-2 imagery. Geocarto Int. 32, 1389–1406.
1004     doi:10.1080/10106049.2016.1213888

1005 Shiratsuchi, L., Ferguson, R., Shanahan, J., Adamchuk, V., Rundquist, D., Marx, D., Slater, G., 2011. Water and
1006     Nitrogen Effects on Active Canopy Sensor Vegetation Indices. Agron. J. 103, 1815.
1007     doi:10.2134/agronj2011.0199

1008 Shojanoori, R., Shafri, H.Z.M., Mansor, S., Ismail, M.H., 2016. The Use of WorldView-2 Satellite Data in
1009     Urban Tree Species Mapping by Object-Based Image Analysis Technique. Sains Malaysiana 45, 1025–
1010     1034.

1011 Siegmann, B., Jarmer, T., Lilienthal, H., Richter, N., Selige, T., Sensing, R., 2012. Comparison of Narrow Band
1012     Vegetation Indices and Empirical Models From Hyperspectral Remote Sensing Data for the Assessment of
1013     Wheat Nitrogen Concentration.

1014 Sokolova, M., Japkowicz, N., Szpakowicz, S., 2006. Beyond Accuracy, F-Score and ROC: A Family of
1015     Discriminant Measures for Performance Evaluation 1015–1021. doi:10.1007/11941439_114

1016 Srestasathiern, P., Rakwatin, P., 2014. Oil Palm Tree Detection with High Resolution Multi-Spectral Satellite
1017     Imagery. Remote Sens. 6, 9749–9774. doi:10.3390/rs6109749

1018 Sripada, R.P., Schmidt, J.P., Dellinger, A.E., Beegle, D.B., 2008. Evaluating Multiple Indices from a Canopy
1019     Reflectance Sensor to Estimate Corn N Requirements. Agron. J. 100, 1553. doi:10.2134/agronj2008.0017

1020 Tardi, A., 2014. The culinary uses of extra-virgin olive oil, in: Peri, C. (Ed.), The Extra-Virgin Olive Oil
1021     Handbook. Wiley-Blackwell, Oxford, UK, p. 380.

1022 Tucker, C.J., 1979. Red and photographic infrared linear combinations for monitoring vegetation. Remote Sens.
1023     Environ. 8, 127–150. doi:10.1016/0034-4257(79)90013-0

1024 Vanonckelen, S., Lhermitte, S., Balthazar, V., Van Rompaey, A., 2014. Performance of atmospheric and
1025     topographic correction methods on Landsat imagery in mountain areas. Int. J. Remote Sens. 35, 4952–
1026     4972. doi:10.1080/01431161.2014.933280

1027 Veroustraeate, F., Sabbe, H., Eerens, H., 2002. Estimation of carbon mass fluxes over Europe using the C-Fix
1028     model and Euroflux data. Remote Sens. Environ. 83, 376–399. doi:10.1016/S0034-4257(02)00043-3

1029 Villalobos, F.J., Testi, L., Hidalgo, J., Pastor, M., Orgaz, F., 2006. Modelling potential growth and yield of olive
1030     (Olea europaea L.) canopies. Eur. J. Agron. 24, 296–303. doi:10.1016/j.eja.2005.10.008

1031 Vincini, M., Frazzi, E., D'Alessio, P., 2008. A broad-band leaf chlorophyll vegetation index at the canopy scale.
1032     Precis. Agric. 9, 303–319. doi:10.1007/s11119-008-9075-z

1033 Vossen, P., 2007. Olive Oil: History, Production, and Characteristics of the World's Classic Oils. HortScience
1034     42, 1093–1100.

1035 Wallace, J.F., Caccetta, P.A., Kiiveri, H.T., 2004. Recent developments in analysis of spatial and temporal data
1036     for landscape qualities and monitoring. Austral Ecol. 29, 100–107. doi:10.1111/j.1442-9993.2004.01356.x

1037 Wang, L., Gong, P., Biging, G.S., 2004. Individual Tree-Crown Delineation and Treetop Detection in High-
1038     Spatial-Resolution Aerial Imagery. Photogramm. Eng. Remote Sens. 70, 351–357.
1039     doi:10.14358/PERS.70.3.351

1040 Waser, L.T., Küchler, M., Jütte, K., Stampfer, T., 2014. Evaluating the potential of worldview-2 data to classify
1041     tree species and different levels of ash mortality. Remote Sens. 6, 4515–4545. doi:10.3390/rs6054515

1042 Wojtowicz, M., Wojtowicz, A., Piekarczyk, J., 2016. Application of remote sensing methods in agriculture.
1043     Commun. Biometry Crop Sci. 11, 31–50.

1044 Wolf (né Straub), B.-M., Heipke, C., 2007. Automatic extraction and delineation of single trees from remote
1045     sensing data. Mach. Vis. Appl. 18, 317–330. doi:10.1007/s00138-006-0064-9

1046 Wolf, A.F., 2012. Using WorldView-2 Vis-NIR multispectral imagery to support land mapping and feature
1047     extraction using normalized difference index ratios. Proc. SPIE 8390, 83900N-83900N–8.
1048     doi:10.1117/12.917717

1049 Ye, B., Tian, S., Ge, J., Sun, Y., 2017. Assessment of WorldView-3 data for lithological mapping. Remote Sens.
1050     9, 1–19. doi:10.3390/rs9111132

1051 Zar, J.H., 1996. Biostatistical analysis, 3rd editio. ed. Prentice Hall International, London.

1052 Zarco-Tejada, P.J., Miller, J.R., Morales, A., Berjón, A., Agüera, J., 2004. Hyperspectral indices and model
1053     simulation for chlorophyll estimation in open-canopy tree crops. Remote Sens. Environ. 90, 463–476.

1054          doi:10.1016/j.rse.2004.01.017

1055    Zartaloudis, Z., Savvidis, G., Savvidis, K., Iatrou, M., Glavenas, D., 2015. Early and timely detection of
1056          Verticillium dahliae in olive growing using remote sensing, in: El Aceite de Oliva. Actas Simposio
1057          Expoliva 2015. Jaén (Espana), p. 7.

1058    Zheng, G., Moskal, L.M., 2009. Retrieving Leaf Area Index (LAI) Using Remote Sensing: Theories, Methods
1059          and Sensors. Sensors 9, 2719–2745. doi:10.3390/s90402719

**Fig. 11.** Study areas localization based on high spatial resolution WorldView-3 satellite images presented in true color band combination (RGB 5-3-2) (Acquisition date: A, 24 June 2016; B, 2 July 2016).

**Fig. 12.** A synthetic flow-chart showing the implemented semi-automated processing workflow to derive vegetation indices (VIs) at tree crown details from WordlView-3 (WW3) imagery.

**Fig. 13.** Geographic object-based image analysis (GEOBIA) sequenced feature model process nodes for the extraction of olive tree crowns. (I): a subset of the corrected WorldView-3 (WV-3) satellite imagery, presented in a false infrared color band combination (RGB 7-5-3); (II): raster pixel processor; (III): raster object creator; (IV-V): raster object operators; (VI): rater to vector conversion; (VII): vector object operator; (VIII): vector object processor; (IX): extracted olive tree crown boundaries [yellow line] overlapped on the input image.

**Fig. 14.** WV-3 scene subset of the two olive orchards (acquisition date[A] 24 June 2016; [B] 2 July 2016)) showed with vegetation enhancement color band combination (RGB 7-6-5). In each study area, in red, are highlighted the four plots defined for accuracy assessment of geographic object-based image classification (GEOBIA) and for statistical analyses of spectral behavior of olive trees [Top left, study area A. Top right, study area B. Down left and down right, image detail of plot $A_2$ and $B_1$, respectively, with superimposed (in yellow) the polygonal boundaries of tree crowns obtained through GEOBIA classification and extraction].

**Fig. 15.** Relationship between number of reference trees and number of correctly detected trees in the eight investigation plots.

**Fig. 16.** Vegetation indices (VIs) maps of study area A

**Fig. 17.** Vegetation indices (VIs) maps of study area B

**Fig. 18.** Maps of Normalized Difference Red Edge (NDRE) and Modified Chlorophyll Absorption Ratio Index Improved (MCARI2) Vegetation indices (VIs) at tree crown detail of study area A.

**Fig. 19.** Maps of Normalized Difference Red Edge (NDRE) and Modified Chlorophyll Absorption Ratio Index Improved (MCARI2) Vegetation indices (VIs) at tree crown detail of study area B

**Fig. 20.** Box-and-whisker plots of single WV-3 bands reflectance values variability in each study area plot (A1-A4 and B1-B4).

**Table captions**

**Table 11 -** WorldView-3 sensor wavelength bands [nm] and relative ground sample distance [GSD] details
1088 (centered wavelength in brackets).

1089 **Table 12 -** Formulation of the five vegetation indices (VIs) used in the present research.

1090 **Table 13 -** Accuracy assessment of classified study area images derived from GEOBIA and olive sample trees
1091 cue metrics [(± n): ± st.dev].

1092 **Table 14 -** Results and accuracy indicators of the olive tree crown extraction (TP, true positive; FP, false
1093 positive; FN, false negative; *r*, recall; *p*: precision).

1094 **Table 15 -** Univariate statistics of Vegetation indices (VIs) map values, for each plot, inside A and B study areas

1095 **Table 16** - Pairwise correlations among the eight bands of WorldView-3 (WV-3) imagery, computed from the
1096 reference sample trees of A study area. Correlation values are given in the lower triangle of the matrix, and the
1097 two-tailed probabilities are given in the upper (Correlations >0.75 in bold letters, ns: no significance; *p<0.01,
1098 **p<0.05).

1099 **Table 17 -** Pairwise correlations among the eight bands of WorldView-3 (WV-3) imagery, computed from the
1100 reference sample trees of B study area. Correlation values are given in the lower triangle of the matrix, and the
1101 two-tailed probabilities are given in the upper (Correlations >0.75 in bold letters, ns: no significance; *p<0.01,
1102 **p<0.05).

1103 **Table 18 -** Summary of normality, homoscedasticity tests and ANOVA statistics result of all grouped band
1104 reflectance value, among all A plots. Summary of post-hoc test for significant band comparison [ns: no
1105 significance; different letters indicate the different plots where single band reflectance values significantly differ
1106 (p < 0.05)].

1107 **Table 19.** Summary of normality, homoscedasticity tests and ANOVA statistics result of all grouped band
1108 reflectance value, among all B plots. Summary of post-hoc test for significant band comparison [ns: no
1109 significance; different letters indicate the different plots where single band reflectance values significantly differ
1110 (p < 0.05)].